AFRL-VS-PS-
TR-2007-1015

Chalcogenide Materials Fabrication and Initial Characterization for Reconfigurable Interconnect Technology

P. Craig Taylor

University of Utah
Department of Physics
115 South I400 East
Salt Lake City, UT 84112

1 October 2006

Final Report

AIR FORCE RESEARCH LABORATORY
Space Vehicles Directorate
3550 Aberdeen Ave SE
AIR FORCE MATERIEL COMMAND
KIRTLAND AIR FORCE BASE, NM 87117-5776

NOTICE AND SIGNATURE PAGE

Using Government drawings, specifications, or other data included in this document for any purpose other than Government procurement does not in any way obligate the U.S. Government. The fact that the Government formulated or supplied the drawings, specifications, or other data does not license the holder or any other person or corporation; or convey any rights or permission to manufacture, use, or sell any patented invention that may relate to them.

This report was cleared for public release by the Air Force Research Laboratory Space Vehicles Directorate, Public Affairs Office and is available to the general public, including foreign nationals. Copies may be obtained from the Defense Technical Information Center (DTIC) (http://www.dtic.mil).

AFRL-VS-PS-TR-2007-1015 HAS BEEN REVIEWED AND IS APPROVED FOR PUBLICATION IN ACCORDANCE WITH ASSIGNED DISTRIBUTION STATEMENT.

//signed//

ARTHUR EDWARDS
Program Manager

//signed//

JOHN P. BEAUCHEMIN, Lt Col, USAF
Deputy Chief, Spacecraft Technology Division
Space Vehicles Directorate

This report is published in the interest of scientific and technical information exchange, and its publication does not constitute the Government's approval or disapproval of its ideas or findings.

REPORT DOCUMENTATION PAGE

Form Approved
OMB No. 0704-0188

1. REPORT DATE *(DD-MM-YYYY)*	2. REPORT TYPE	3. DATES COVERED *(From - To)*
01/10/2006	Final Report	01/10/2003 to 01/10/2006

4. TITLE AND SUBTITLE
Chalcogenide Materials Fabrication and Initial Characterization for Reconfigurable Interconnect Technology

5a. CONTRACT NUMBER
F29601-03-1-0229

5b. GRANT NUMBER

5c. PROGRAM ELEMENT NUMBER
62601F

6. AUTHOR(S)
P. Craig Taylor

5d. PROJECT NUMBER
4846

5e. TASK NUMBER
RP

5f. WORK UNIT NUMBER
A1

7. PERFORMING ORGANIZATION NAME(S) AND ADDRESS(ES)

University of Utah
Department of Physics
115 South I400 East
Salt Lake City, UT 84112-0830

8. PERFORMING ORGANIZATION REPORT NUMBER
UU-04

9. SPONSORING / MONITORING AGENCY NAME(S) AND ADDRESS(ES)
Air Force Research Laboratory
Space Vehicles Directorate
3550 Aberdeen Ave., SE
Kirtland AFB, NM 87117-5776

10. SPONSOR/MONITOR'S ACRONYM(S)
AFRL/VSSE

11. SPONSOR/MONITOR'S REPORT NUMBER(S)
AFRL-VS-PS-TR-2007-1015

12. DISTRIBUTION / AVAILABILITY STATEMENT
Approved for public release; distribution is unlimited. (Clearance #VS07-0122).

13. SUPPLEMENTARY NOTES
This report is published in the interest of scientific and technical information exchange. The established procedures for editing reports were not followed for this technical report.

14. ABSTRACT

The optical properties of sputtered, amorphous films of GeTe, Sb2Te3, and Ge2SbTe5 grown up to several micrometers thick are influenced by the presence of oxygen impurities. The absorption edges in these glasses are sometimes broader than in standard chalcogenide glasses, such as GeSe2 and As2Se3. This result implies either that the valance band consists of high strained bonds or that large densities of defects exist. Below the optical gap the refractive index for Ge2Sb2Te5 is approximately 3.5.

In samples of Ge2Sb2Te5 made with large oxygen concentrations using a hot-pressed target, there exists a large ESR signal corresponding to a defect density of 10^19 cm^-3. In samples with the lowest oxygen contamination levels (approximately 10^19 cm^-3) no ESR signal is observed, which implies that the defect density is below 10^18 com^-3. ESR signals associated with the glassy SiO2 interface with the chalcogenide films are also observed.

In amorphous Ge2Sb2Te5, the average coordination numbers for Ge, Sb, and Te are approximately 4, 3, and 2.5 respectively.

15. SUBJECT TERMS
Ge2Sb2Te5, chalcogenide films

16. SECURITY CLASSIFICATION OF:			17. LIMITATION OF ABSTRACT	18. NUMBER OF PAGES	19a. NAME OF RESPONSIBLE PERSON
a. REPORT	b. ABSTRACT	c. THIS PAGE			Arthur Edwards
Unclassified	Unclassified	Unclassified	Unlimited	52	19b. TELEPHONE NUMBER *(include area code)* (505) 853-6042

Standard Form 298 (Rev. 8-98)
Prescribed by ANSI Std. 239.18

Final Performance Report of F29601-03-01-0229

CHALCOGENIDE MATERIALS FABRICATION AND INITIAL CHARACTERIZATION FOR RECONFIGURABLE INTERCONNECT TECHNOLOGY

P. C. Taylor

University of Utah
Department of Physics
115 South 1400 East, Room 201
Salt Lake City, UT 84112-0830

I. INTRODUCTION

Amorphous and crystalline films in the system Ge-Sb-Te are of interest because of their use in reversible phase change optical storage media. "Phase change" applications utilize differences in optical or electrical properties between the crystalline and amorphous phases of the same material. Optical storage applications utilize small differences (approximately 20%) in the reflectivity [1], while electronic applications utilize large differences (factors of approximately 10^3) in electrical conductivity [2]. In this technology, the most commonly employed composition is $Ge_2Sb_2Te_5$, which lies along the pseudobinary tie line GeTe-Sb_2Te_3. Although films of $Ge_2Sb_2Te_5$ are employed in rewritable digital versatile disks (DVD's), little is known about the structural, optical and electronic properties of this material, especially in the amorphous phase.

In this paper we present data on amorphous films of GeTe, Sb_2Te_3, and $Ge_2Sb_2Te_5$ grown by rf sputtering. First we review some features of the local structural order in glassy $Ge_2Sb_2Te_5$ [3]. Next we examine the effects of oxygen impurities on the optical and electronic properties of amorphous GeTe, Sb_2Te_3, and $Ge_2Sb_2Te_5$. Finally we identify some characteristic defects that occur on growth in these three amorphous solids.

II. A SIMPLE MODEL OF THE STRUCTURE OF $Ge_xSb_yTe_{1-x-y}$ GLASSES

The structure of glassy $Ge_2Sb_2Te_5$ is not well known, but one may speculate concerning the local structural order using simple rules derived from the primarily covalent nature of the bonding [3]. If only s- and p-electrons are considered in the bonding, then one may calculate the average local coordination number for any given ternary glass composition if the coordination numbers of two of the three elemental constituents are known [4,5,6]. This possibility arises because the number of bonds for a given atom, n_b, is related to the number of s and p valence electrons (column number in the periodic table), N, by the equation, $n_b = 8 - N$. This relation is sometimes called the "8-N rule" [7].

In the case of glassy $Ge_2Sb_2Te_5$, recent extended x-ray absorption fine structure (EXAFS) experiments suggest that the Ge and Sb atoms are probably 4- and 3-fold coordinated, respectively [8,9]. If the coordination number for Te is always two (the 8-N rule holds for all three elements individually), then one may calculate the average coordination number for all glasses in the system. This is the situation that holds in the Ge-As-Se ternary system [6]. We consider the normalized composition, $Ge_xSb_yTe_{1-x-y}$, where x and y are between zero and one. In this case the average coordination number, n_{av}, is

$$n_{av} = 2x + y + 2 . \qquad (1)$$

Equation (1) applies when there is little or no preference for specific chemical bonds [6]. The $Ge_xSb_ySe_{1-x-y}$ system is a good example of this situation. In this case there is little preference for specific bonds so that the Se remains two-fold coordinated at all compositions, and off the "pseudo-binary" line, $GeSb_2$-Sb_2Se_3, where there are only Ge-Se and Sb-Se bonds, additional bonds, such as Sb-Sb, Ge-Ge, and Se-Se, occur [3].

A second possibility is that the coordination number of Te increases with increasing Ge and Sb concentration to insure that only Ge-Te and Sb-Te bonds occur at all possible

compositions. This situation, which occurs when there is a strong chemical preference for specific bonds, is analogous to the one that holds in the Cu-As-Se and Cu-As-S ternary systems where the Cu is always tetrahedrally coordinated [10,11]. In the latter case the average coordination number is the same as that given in eq. (1) for $6x + 5y < 2$ (to the left of the dotted line in Fig. 1). To the right of this line the average coordination number for Te increases from two to three. Along the pseudo-binary line $7x + 6y = 3$, which is not shown in Fig. 1,the average coordination number for Te is three. The composition $Ge_2Sb_2Te_5$ lies just to the left of this line so the average coordination number for Te is slightly less than three.

In addition to the pseudo-binary line, $GeTe_2$-Sb_2Te_3, where the Te is always 2-fold coordinated and there are only Ge-Te and Sb-Te bonds (dotted line), Figure 1 shows two other pseudo-binary lines. The solid line, GeTe-Sb_2Te_3, contains the $Ge_2Sb_2Te_5$ composition (2GeTe-Sb_2Te_3). It follows from eq. (1) that if Te is two-fold coordinated, there must be some additional bonds (Ge-Ge, Sb-Sb, or perhaps Ge-Sb) along the line GeTe-Sb_2Te_3, which contains insufficient Te to satisfy the constraint of only Ge-Te and Sb-Te bonds. The third dashed line $GeTe_2$-Sb_2Te shows the compositions where the average coordination number is invariant and equal to that in $Ge_2Sb_2Te_5$ if the Te remains two-fold coordinated. This line is potentially important because in some ternary systems, such as Ge-As-Se, many properties of the glass are dependent only on the average coordination number and independent of the specific chemical composition [12]. This phenomenon is sometimes referred to as the "iso-coordination" rule [12].

Given the above discussion, there are two possibilities for bonding in the $Ge_2Sb_2Te_5$ alloy [3]. First, if eq. (1) holds, then the Te is 2-fold coordinated and either 1/3 of the Ge bonds are Ge-Ge bonds, or ½ of the Sb-bonds are Sb-Sb bonds, or some mixture of these two possibilities, and $n_{av} = 2.67$ [3]. (From EXAFS measurements, there is no experimental evidence for the

presence of Ge-Sb bonds [8,9].) Second, if n_{av}^{Te} increases to keep the constraint of only Ge-Te and Sb-Te bonds, then $n_{av}^{Te} = 2.8$ and $n_{av} \cong 3.1$ [3]. The current experimental evidence from EXAFS is insufficient to distinguish between these two possibilities.

Not all glasses are homogeneous. In the Group IV-V-VI ternaries, it has been suggested that phase separation, on length scales < about 100 nm, can occur whenever there exists enough Ge to separate into $GeTe_x$ ($x < 2$) and Sb_2Te_3 regions [13]. This situation holds anywhere to the right of the $GeTe_2$-Sb_2Te_3 tie line in Fig. 1 (dotted line). In the Ge-As-Se system such phase separation occurs only near the "edges" of the diagram (Ge-Se and As-Se lines) [13]. Whether or not there is small-scale phase separation for the composition $Ge_2Sb_2Te_5$ is presently unclear, but the composition $Ge_2Sb_2Te_5$ lies on the line representing those compositions that are least likely to phase separate [3].

III. EXPERIMENTAL DETAILS

Amorphous films of GeTe, Sb_2Te_3, and $Ge_2Sb_2Te_5$ were sputtered using quartz (Quartz Scientific), aluminum foil (Alcoa Inc.), and glass microscope slides (Fisher Scientific) as substrate materials. Each substrate was hand washed with diluted Micro-90 soap (Cole-Parmer Instrument Company), rinsed with deionized water, and then washed first in acetone for 20 minutes and then in ethanol for 20 minutes in a Branson 1510 ultrasonic cleaner (Branson Ultrasonics). Following the ethanol wash, each substrate was rinsed in ethanol, dried with nitrogen gas, and placed directly into the sputtering chamber. Thin film samples of GeTe, Sb_2Te_3, and $Ge_2Sb_2Te_5$ were then sputtered using a Perkin Elmer Randex 3140 rf sputtering system.

Ingots of GeTe, Sb_2Te_3, and $Ge_2Sb_2Te_5$, weighing 12 to 20 g, were prepared at the Optoelectronic Materials Laboratory at the University of Utah. Starting materials were 6N Ge

(ESPI), 6N Sb (Honeywell) and 6N Te (Atomergic Chemetals). Mixtures of the elements were typically melted and rocked at 770 C for approximately 15 hours. They were then cast into the desired target geometry using specially prepared quartz ampoules. Individual targets were then attached to oxygen free, high conductivity copper electrodes (backing plates) using EPO-TEK 410E electrically conductive silver epoxy (Epoxy Technology, Inc.). The targets and backing plates were then cured under vacuum for 1 hour at 150 °C. [Initial samples were made using targets that were hot-pressed from powdered material, but the resulting films contained excessive concentrations of oxygen so the results presented in the present work are primarily for samples made using targets cast from melted and rocked ingots.]

The films were deposited onto substrates nominally at room temperature. Growth rates were varied from approximately 0.75 Å/s (corresponding to an rf power of 7 W) to approximately 6 Å/s (rf power of 50 W). The Ar pressure was 15 mTorr. Film thicknesses varied from approximately 0.3 μm to 3 μm.

Secondary ion mass spectroscopy (SIMS) was performed [Evans East] on films grown at several different growth rates to obtain a precise measurement of the amount of oxygen present in the sputtered samples. Typically, SIMS is able to detect impurities, such as oxygen, on the order of parts per million with an absolute accuracy of about a factor of two.

Optical absorption measurements were performed on the films using photothermal deflection spectroscopy (PDS) [14]. This calorimetric technique allows absorption to be measured to low levels in thin film samples. For films whose thicknesses are approximately 1 μm, absorption coefficients, α, can be measured down to approximately 0.1 cm^{-1} [14], which is more than sufficient for the present experiments. For films whose thicknesses are known,

interference “fringes” in the PDS spectra were used to determine the index of refraction below the optical band gap.

Paramagnetic defects in these films were measured using electron paramagnetic resonance (electron spin resonance, or ESR) spectroscopy. The spectrometer employed was a Bruker, Model EMX, which operated at x-band (nominally 9 GHz). Measurements were performed at variable temperatures between 4 and 300 K. Variable temperatures were obtained using a Helitran helium-flow system. Spin densities were estimated by comparison with a standard sample (weak pitch). Details are available elsewhere [15].

Both x-ray and x-ray absorption fine structure (EXAFS) experiments [9] confirmed that the films are essentially all amorphous. Conductivity measurements in the co-planar geometry yield values much greater than measurements on the same sample in the sandwich geometry. The probable reason for this discrepancy is that there exists a thin crystalline layer in the $Ge_2Sb_2Te_5$ films at the substrate-film interface. This layer effectively shorts the conductivity measurements in the co-planar geometry but has only minimal effect on the measurements in the sandwich geometry. There is also evidence for small concentrations (< 1 at. %) of crystallinity in GeTe, Sb_2Te_3, and $Ge_2Sb_2Te_5$ from the EXAFS experiments [9].

Thick (> 1 μm) amorphous films were optically crystallized so that the structure could be probed by EXAFS experiments. A 100 fs pulsed 532 nm laser (frequency doubled YAG laser), pulsed at a repetition rate of 76 MHz, was focused onto the sample with a microscope objective to a spot size of approximately 20 microns in diameter. Each pulse train was 13.16 nanoseconds long with a power density from 80 kW/cm2 to 160 kW/cm2. The sample was moved under the beam by a pair of computer controlled linear stages such that an area of a few square millimeters

was exposed. The sample sat on a copper heat sink through which circulated cold water to facilitate cooling.

IV. EFFECT OF GROWTH CONDITIONS ON OPTICAL AND ELECTRONC PROPERTIES

Films grown using targets that were hot pressed from powdered bulk samples exhibited excessive oxygen contamination on the order of 10^{21} to 10^{22} cm^{-3}. This excessive oxygen contamination is probably due to oxidized surfaces in the hot-pressed target. For this reason we report mostly results for films made using targets slumped from cast ingots. Even using cast targets, films grown at different growth rates exhibited vastly different concentrations of oxygen impurities. Typical results are shown in Table I. Samples of $Ge_2Sb_2Te_5$ grown from a cast target at the fastest growth rate (approximately 6 Å/s) showed the lowest oxygen concentrations of approximately 10^{19} cm^{-3}. A typical SIMS spectrum for such samples is shown in Fig. 2.

Optical absorption spectra measured by PDS for amorphous films of GeTe, Sb_2Te_3, and $Ge_2Sb_2Te_5$ grown at 6 Å/s are shown in Fig. 3. The optical energy gaps estimated from the energies where the optical absorption coefficients $\alpha = 10^4 cm^{-1}$ are, respectively, E_{04} = 0.9, ~0.4, and 0.8 eV for GeTe, Sb_2Te_3, and $Ge_2Sb_2Te_5$ grown at 6 Å/s. The optical gaps, denoted as E_{04}, for several chalcogenide crystals and glasses are shown in Table II.

We first present the trends for amorphous $Ge_2Sb_2Te_5$ and GeTe where the dependences of the optical absorption spectra on growth rates are shown in Fig. 4 and Fig. 5, respectively. Two trends are apparent from the data shown in Fig. 4. First, the optical gap decreases with increasing growth rate, and second, the inverse slopes of the exponential band tails (Urbach tails) extending into the gap increase with increasing growth rate. [The parameter ΔE characterizes the

inverse band-tail slope according to the relation $\alpha \propto e^{E/\Delta E}$.] Because the oxygen concentration is a strong function of the growth rate, it is unclear apriori whether these trends are due to the growth rate or the oxygen incorporation in the films. Figure 6 shows these trends as a function of oxygen concentration explicitly for the films of $Ge_2Sb_2Te_5$ (solid and open circles). The values for E_{04} were estimated from the data in Fig. 6 by subtracting off the exponential band tail absorption contribution. The smaller the value of ΔE the steeper the slope of the exponential absorption tail. The sample with maximum oxygen concentration was grown at 6 Å/s using a hot-pressed target. We have excluded the data for E_{04} and ΔE for this sample because the Urbach absorption tail in this sample was so broad ($\Delta E = 120$ meV) that it made the determination of E_{04} very inaccurate. The increase of the optical gap for oxygen concentrations greater than about 10^{21} cm^{-3} is probably due to the presence of oxygen at levels approaching alloy compositions. On the other hand, the sharpening of the band tail absorption could be due to a relaxation of the amorphous lattice with increasing oxygen concentration (decrease of the average nearest-neighbor coordination number) or to increased diffusion of the atoms on the surface during growth with decreasing growth rate. We favor the latter explanation because the sample with the greatest oxygen concentration, which was grown using the hot-pressed target, has the broadest band-tail absorption. This sample does not follow the trend shown in Fig. 6 for the samples grown using the cast target.

Because the optical band gap usually scales inversely with the index of refraction measured well below the gap, one can also use values of the index to estimate optical band gaps. Figure 7 shows the variation of *n* with oxygen concentration (or growth rate). The point with maximum oxygen concentration was obtained from a sample grown using a hot-pressed target. This figure shows clearly that the presence of oxygen at levels greater than about an atomic

percent produces a sharp increase in the optical energy gap. This is not surprising since the oxides of Ge, Sb, and Te all have energy gaps much greater than that of $Ge_2Sb_2Te_5$.

Similar trends are seen for amorphous GeTe and Sb_2Te_3, but the variations in optical gaps and band-tail slopes are less prominent. [Because of the limitations of our PDS equipment, we were unable to measure accurately the band-tail optical absorption in Sb_2Te_3.] The major reason for this relative independence on growth rate is probably because the oxygen concentration remains high at all growth rates for these two compositions as shown in Table I. For both GeTe and Sb_2Te_3 the oxygen concentration never drops below 10^{20} cm^{-3}. The optical absorption spectra for amorphous GeTe at two different growth rates (6 and 3 Å/s) are shown in Fig. 5. The values of E_{04} and ΔE extracted from these spectra are shown, respectively, as solid and open squares in Fig. 6. Because the values of ΔE for GeTe are well above those for $Ge_2Sb_2Te_5$ for similar oxygen concentrations, we again speculate that the narrowing of the band-tail absorption in $Ge_2Sb_2Te_5$ is the result of slower growth rates rather than greater oxygen concentrations.

Table I shows the oxygen concentrations in GeTe, Sb_2Te_3, and $Ge_2Sb_2Te_5$ as a function of growth rate. For GeTe and Sb_2Te_3 the oxygen concentrations are relatively independent of growth rate and never fall below 10^{20} cm^{-3}, even at the fastest growth rate. For $Ge_2Sb_2Te_5$, however, the oxygen concentration is approximately 10^{19} cm^{-3} at the fastest growth rate of 6 Å/s.

We next describe the paramagnetic defects present in amorphous GeTe, Sb_2Te_3, and $Ge_2Sb_2Te_5$ as measured by ESR. Figure 8 shows the ESR spectrum at 40 K in amorphous $Ge_2Sb_2Te_5$ made using the hot pressed target (sample 130 of Table I). Although the signal-to-noise ratio of this spectrum is not good, we may speculate as to the origin of the broad signal by analogy with spectra observed in other chalcogenide glasses. [The spectrum shown in Fig. 8 was run at high microwave power and with large magnetic field modulation amplitude to enhance the

possibility to observe broad lines.] In particular, in the absence of hyperfine structure or fine structure, the width of the line is determined by the spin-orbit interaction, which increases dramatically with increasing atomic number. Using this reasoning, the broad line is too broad to be associated with a defect primarily centered at a Ge site, and since there is no evidence of significant hyperfine structure, the line is also unlikely to be primarily centered on an Sb site. The solid line in Fig. 8 is a fit to this feature using values for the g-tensor that are scaled from chalcogenide glasses where the observed ESR centers are primarily centered on Se and S sites [16]. By scaling with the spin-orbit coupling constants [17, 18] for S, Se, and Te, we obtain principal g-values for the Te site of 2.00, 2.07, and 2.33. Strictly speaking, the g-values come from the assumption that the wave functions for the ground and excited states of the unpaired spin on the Te are the same as they are for the same site on S and Se. In the case of the S- and Se-based glasses this assumption is approximately correct [16]. In these systems, the paramagnetic center is a hole on the chalcogen atom, which is predominantly localized on a p-orbital [16]. Clearly the solid line in Fig. 9 is not a "fit" to the data but rather a plausible guess at the approximate lineshape.

The lineshape shown by the solid line in Fig. 8 is the result of a "powder" average over all sites that are randomly oriented with respect to the applied magnetic field. This lineshape, which is known as a powder pattern, has been convoluted with a Gaussian isotropic broadening function of width 35 G to approximate the unresolved interactions, such as the dipole-dipole interactions [19]. The strongest feature of the experimental spectrum in Fig. 8 is captured well by the fit, but there is a feature near 2900 G, which is completely absent. This feature is due to the influence of the largest g-value (2.33). In hole centers of this type centered on O, S, and Se it is well established that the largest g-value takes on many values because of the distortions in the

local bonding from site to site in the glass [16,20]. These distortions often wash out the resolved structure that one would expect from a unique site [20]. We speculate that a similar situation occurs for the Te hole centers in glassy $Ge_2Sb_2Te_5$.

By comparison with a standard sample, the signal associated with Te hole centers corresponds to approximately 10^{19} spins cm^{-3}. In the "standard" chalcogenide glasses, such as $GeSe_2$, As_2S_3, and As_2Se_3, no ESR signal is observed until the samples are irradiated with band-gap light at low temperatures [16]. We comment on this important distinction in the next section.

In the S- and Se-based chalcogenide glasses there usually occurs a compensating paramagnetic electron center at densities comparable to those of the hole centers. We find no evidence for such sites localized on Ge atoms at comparable densities. For sites localized on Ge atoms, the dominant g-value is approximately 2.02-2.04 based on ESR centers associated with Ge in amorphous Ge [21], GeS_2 [22], and $GeSe_2$ [23]. If the compensating electron centers were predominantly localized at Sb sites, as they are in the As-chalcogenide glasses, we could not detect them given the current signal-to-noise ratios. The reason is that an electron trapped primarily on an Sb site will undergo a strong hyperfine interaction with either ^{121}Sb or ^{123}Sb, whose nuclear spins are 5/2 and 7/2, respectively. By analogy with the electron centers observed in As-chalcogenide glasses and in amorphous As, whose wave functions contain about 95% p-character and approximately 5% s-character, one can simulate the expected spectrum. Once again this simulation assumes that the wave functions are essentially the same for the As and Sb centers. Because the lineshape is dominated by the hyperfine interaction, the g-value can be taken to be isotropic and equal to the free-electron value ($g = 2.00$). Because the bonding is predominantly via p-orbitals, the hyperfine tensors can be taken to be axial [16]. As scaled from

the known values for ^{75}As, these values for ^{121}Sb and ^{123}Sb are $A_{\parallel} = 588$ G, $A_{\perp} = 246$ G and $A_{\parallel} = 445$ G, $A_{\perp} = 186$ G, respectively [17]. The simulation yields broad features near 2300 and 4400 G, which are too weak in comparison with the Te center to be observed. We have therefore not included this more complicated simulation in Fig. 8.

There are two additional features in the spectrum shown in Fig. 8, a sharp feature near 3350 G and a very sharp feature near 3390 G. Neither feature is captured by the simulation. The very sharp feature is due to E' centers, which occur at the interface between the quartz substrate and the chalcogenide glass film. [The E' center is a standard defect in SiO_2, which is due to an electron trapped in an sp^3 orbital of a 3-fold coordinated Si. The Si is bonded to three O atoms.] The second feature is consistent with an electron center at a Ge site [21], but the data are insufficient to do more than speculate concerning this attribution. In any case, the density of these centers is at least an order of magnitude less than that of the Te-based center, and therefore this center cannot compensate for the Te-based hole center.

When the films are grown using cast targets, the signal related to Te and that tentatively attributed to Ge are not observed. We can place an upper bound on the density of these sites at $\leq 10^{18}$ cm^{-3}. There are, however, other features that do appear as shown in Fig. 9. The top trace in Fig. 9 is a sample of $Ge_2Sb_2Te_5$ grown at 3 Å/s using the cast target; the middle trace is $Ge_2Sb_2Te_5$ grown at 6 Å/s using the cast target; the bottom trace is $Ge_2Sb_2Te_5$ grown at 6 Å/s using the hot-pressed target. The spectra shown in Fig. 9 were taken at lower microwave power and lower magnetic field modulation amplitude than that of Fig. 8. These parameters accentuate the narrower features; however, the lineshape of the very narrow E' center is still distorted. For this reason, the bottom trace in Fig. 9 looks different from the trace shown in Fig. 8. In particular, the feature near 3350 G, tentatively attributed to a center localized at a Ge site, is

more pronounced. The sharp feature in Fig. 9 is the E' center that is also seen in Fig. 8. The additional structure in the spectra shown in Fig. 9 is shown more clearly on an expanded magnetic field scale in Fig. 10. The top trace in both figures is the same ($Ge_2Sb_2Te_5$ grown at 3 Å/s using the cast target). The spectra labeled b and c in Fig. 10 are, respectively, for Sb_2Te_3 and GeTe grown at 6 Å/s using the cast targets.

We will show that all of these features in the films grown using cast targets are probably due to the interface between the chalcogenide films and the glassy SiO_2 substrates. First, the bottom spectrum in Fig. 10 (d) is a simulation using the known g-values for the E' center and a predominant, oxygen-related hole center commonly observed in glassy SiO_2. [The principal g-values for the E' and oxygen hole center are 2.0003, 2.0006, 2.0017 and 2.000, 2.010, and 2.078, respectively [20].] As mentioned above, these hole centers typically have a wide distribution of the largest g-values due to distortions in the local bonding configurations. This distribution washes out the sharp peak in the simulation at approximately 3260 G and introduces a gradually rising intensity, such as that seen in the three experimental spectra. This intensity is most easily seen in spectrum (a) where the baseline is shown as a dotted line. Given this complication, the simulated spectrum fits the observed spectra very well.

Second, the intensities of these features scale with the number of films (i.e., with the number of film surfaces) but not with the total volume of the films. This fact indicates that we are looking at a surface effect. Third, a similar signal (E' center only) is usually observed for other amorphous semiconductors grown by plasma-enhanced chemical vapor deposition on glassy quartz substrates [24]. Finally, as shown in Fig. 11, the intensity of this signal is independent of oxygen concentration in the chalcogenide films, and therefore not due to oxygen contamination of the chalcogenide glasses.

Within our experimental accuracy there is no ESR signal due to the bulk of the chalcogenide films of GeTe, Sb_2Te_3 or $Ge_2Sb_2Te_5$, which are grown using the cast targets. Figure 12 shows a comparison of two films of $Ge_2Sb_2Te_5$ grown at 6 Å/s. The top trace was grown using the cast target, and the bottom trace was grown using the hot-pressed target. The oxygen concentrations differ by at least a factor of 10^3. The spectra were both run at high microwave power and large magnetic field modulation amplitude to emphasize broad features. The top trace has been expanded by a factor of 60, but no broad features are apparent. This null result places an upper bound on the spin density for the glasses made using cast targets of 10^{18} spins/cm^3. We shall comment more on this situation in the next section.

In the Ge-Sb-Te ternary films, oxygen is easily incorporated during growth. When oxygen appears at alloying levels (> 1 at. % $\approx 10^{21}$ cm^{-3}), its presence can influence the optical band gap. On the other hand, the exponential absorption edge that is due to localized states at the edges of the conduction and valance bands is probably not influenced by oxygen for two reasons. First, samples of $Ge_2Sb_2Te_5$ grown using the cast target exhibit sharper band tail slopes with increasing oxygen concentrations (decreasing growth rates), but the sample grown at the fastest growth rate using the hot-pressed target exhibits by far the largest oxygen concentration and the broadest distribution of band-tail states. Second, $Ge_2Sb_2Te_5$ and GeTe (Fig. 6) with similar oxygen concentrations exhibit band tail slopes that are very different. Therefore, the sharpening of the band tail in $Ge_2Sb_2Te_5$ with decreasing growth rate is probably due to better ability of the atoms to diffuse on the surface during growth.

Figure 13 shows the band-tail slopes as a function of growth rate for amorphous films of $Ge_2Sb_2Te_5$. Although there is a difference in the magnitude of the band-tail slope between the two samples grown at 6 Å/s using the cast and hot-pressed targets, the trend is consistent. As

mentioned above there is no consistent trend when the same data are plotted as a function of oxygen concentration (Note that only samples made using the cast target are shown in Fig. 6).

The optical band gaps for amorphous and crystalline forms of GeS [25,26], GeSe [27], GeTe [28], Sb_2S_3 [25,29], Sb_2Se_3 [29,30], Sb_2Te_3 [29,31,32,33] and $Ge_2Sb_2Te_5$ [34] are shown in Table II. Also shown for comparison are amorphous As_2S_3 [35], As_2Se_3 [35], and As_2Te_3 [36]. For amorphous GeTe and $Ge_2Sb_2Te_5$ our results agree with those previously published [25]. For amorphous Sb_2Te_3 our value of the optical gap agrees with some authors [31] but is much smaller than that reported by other groups (0.6 to 0.8 eV) [37]. For several reasons, we believe our value is correct. First, scaling the known optical gaps in the series Sb_2S_3, Sb_2Se_3 to Sb_2Te_3 and comparing to the known scaling in the series As_2S_3, As_2Se_3, As_2Te_3, we estimate that the band gap for amorphous Sb_2Te_3 can be no greater than about 0.6 eV. We can only speculate why the larger value of optical band gap exists in the literature. Because of the great propensity of the films to incorporate oxygen, it is possible that these larger gaps are the result of oxygen contamination.

It is very important to determine eventually whether or not there exists an ESR signal in the films of $Ge_2Sb_2Te_5$ in the absence of optical excitation. The reason is that one can distinguish between the traditional chalcogenide glasses where the defects are dominated by a strong, negative electron-electron correlation energy (negative U_{eff}) and those amorphous solids with higher average coordination number, such as amorphous silicon, where the Coulomb repulsion is the only important term. For the materials with negative U_{eff}, there is no ESR in the absence of optical excitation, but a metastable ESR signal is observed at low temperatures after optical excitation with band-gap light. In contrast, for the materials with positive U_{eff}, there is an ESR signal in the absence of optical excitation and there may or may not be an increase in this

signal after optical excitation. Within this context, it is interesting to note that in amorphous arsenic, whose coordination number is three, defects with both positive and negative U_{eff} exist [16,38]. Amorphous arsenic exhibits both an ESR signal in the absence of optical excitation and a metastable increase in this signal after optical excitation at low temperatures.

The negative U_{eff} character of the defects in the standard chalcogenide glasses has been inferred from four general observations: (1) the absence of ESR without optical excitation, (2) the absence of significant optical absorption that dominates over the exponential absorption tail at energies well below the optical energy gap, (3) the metastable presence of both of these features after optical excitation at low temperatures with band-gap light, and (4) the ability to anneal these two features optically (bleach) with light whose energy is greater than about half the optical energy gap. It is the fourth observation that proves conclusively the negative U_{eff} character of the defects since the difference between the band-gap energy needed to create the defects and the half-band-gap energy needed to optically anneal is approximately the energy of the lattice relaxation. Many other properties of the standard chalcogenide glasses are strongly affected by the negative U_{eff} nature of the defects. For example, the transport properties exhibit unique behavior either through the presence of traps that interact strongly with the lattice and control the transport [39] or through the formation of small polarons [40].

We have so far been unsuccessful in generating any changes in the ESR spectrum of $Ge_2Sb_2Te_5$ with optical excitation at low temperatures. However, we also have not observed an ESR signal in the absence of optical excitation in the samples made from the cast target. Therefore, the question of the role of lattice relaxation in controlling the defects in $Ge_2Sb_2Te_5$ remains unanswered.

Finally, we note that the structure of $Ge_2Sb_2Te_5$ may influence the negative or positive U_{eff} character of the defects. If the Te remains two-fold coordinated, then the structure has lower average coordination number and is more like to exhibit negative U_{eff} behavior. On the other hand, if the coordination number approaches three to accommodate the restriction of only Ge-Te and Sb-Te bonds, then the structure has higher coordination number and is more likely to exhibit positive U_{eff} behavior. It is even possible that the coordination number of Te is between these two extremes, and that defects with both positive and negative U_{eff} may coexist.

V. OPTICAL SWITCHING IN THICK FILMS

Figure 14 shows an atomic force microscope (AFM) image of a film of $Ge_2Sb_2Te_5$, which is approximately 1 μm thick. The film was amorphous as grown. The thin stripes, which are approximately 20 μm wide, were optically crystallized using 512 nm light from a pulsed laser source. In the crystallized regions there is an increase in the roughness and an apparent decrease in thickness, which may be due to ablation at the relatively high power densities used. Optically induced crystallization in thinner layers capped with SiO_2 showed no increase in roughness and no ablation. The purpose of these experiments was to provide large-area samples of optically crystallized $Ge_2Sb_2Te_5$ for extended x-ray absorption fine structure (EXAFS) studies [41,42].

VI. "VOIDS" IN THICK FILMS

Figure 15 shows small angle x-ray scattering (SAXS) results on two films of amorphous Ge2Sb2Te5 grown on Al-foil at approximately 6 Å/s and 3 Å/s, respectively. X-ray diffraction (XRD) measurements show that the films are completely amorphous. The SAXS data for the two samples are quite similar. As shown at the bottom of the figure, fitting of a distribution of spheres (solid lines) indicates slight but significant differences in the average size of the scattering features, which are probably voids. Figure 16 compares the tilting effect for the

sample grown at 6 Å/s. Both films showed a significant reduction in SAXS upon tilting, and this behavior demonstrates elongated scattering features with the long axis along the growth direction. This result is not surprising since many amorphous films, especially those grown at high growth rates, exhibit columnar-like structure. The sample grown at 3 Å/s shows a stronger effect so its features are more elongated or more highly aligned along the growth direction. Based on the ratio of integrated intensities at 0^{O} and 45^{O} tilt, and an ellipsoidal model, we estimate the average ratio of major-to-minor axes to be about 7 and 14 for the samples grown at 6 Å/s and 3 Å/s, respectively. Under this model, the diameters shown in Fig. 15 represent the minor-axis diameters of ellipsoids of revolution rather than spheres.

VI. PHOTO-OXIDATION AND THE ABSENCE OF PHOTODARKENING

Figure 17 displays the depth profile of oxygen obtained by Secondary Ion Mass Spectrometry (SIMS) in 100 nm films of amorphous Ge2Sb2Te5, one of which was illuminated by the filtered near-infrared light for 100 hours. It is evident that infrared illumination enhances the diffusion of oxygen deep into the material. The surface has especially high oxygen content, which can be regarded as the oxide of Ge2Sb2Te5, although there is no sharp interface between the oxide layer and bulk Ge2Sb2Te5. Oxidation did proceed without illumination, but our elipsometry analysis showed that a degree of oxidation equivalent to that in the illuminated sample would require a few months in darkness. When we used the entire spectrum of the light source, (i.e. including visible and near-uv light by removing the long-pass filter), the photo-oxidation became much faster. Therefore, photons having energies much greater than the bandgap can also produce photo-oxidation.

In order to test further the possibility of an optically induced change in the optical constants of Ge2Sb2Te5, additional transparent thin films were deposited on Ge2Sb2Te5 to

block the diffusion of oxygen but allow the transmission of photons. When the sample was coated with 20 nm of sputtered silicon nitride, the elipsometry signals were practically identical before and after 28 hours of illumination. Therefore, we confirm that the change in optical properties of Ge2Sb2Te5 by illumination is negligible [43]. A small but detectable change in the elipsometry data was observed when the top layer was sputter-deposited SiOx, but an additional coating of silicon nitride completely blocked this change. Hence the change of the SiOx-coated film must be caused by the oxidation of Ge2Sb2Te5 by oxygen atoms diffusing from the ambient through the SiOx, rather than by the oxygen in the SiOx layer. Our result indicates that repeated laser illumination on rewritable DVDs would not cause any significant change in optical constants, or migration of oxygen from the SiO2-containing cladding layers to the Ge2Sb2Te5 layer, provided that oxygen diffusion from the ambient is blocked.

The photo-oxidation is presumably the result of free carrier generation in the Ge2Sb2Te5; our finding of room temperature photoconductivity confirms that photo-excited carriers have significant lifetime [44]. The observed absence of photodarkening in Ge2Sb2Te5 is consistent with the tendencies reported in the literature [45]. While light-induced metastable-defect creation seems to be possible in principle in all types of amorphous materials, light-induced structural changes (photodarkening) seem to be restricted to the materials with local structural flexibility resulting from the presence of atoms with low coordination (e.g., two-coordinated chalcogens such as S, Se, and Te). The sensitivity to photodarkening is generally highest for sulfides, somewhat reduced in selenides, and further reduced in tellurides. In addition, the introduction of more highly coordinated constituent atoms, such as Ge, increases the average coordination number and minimizes photostructural effects. Although we only studied the composition Ge2Sb2Te5, the reported change of GexSb20-xTe80 by light [46,47] is qualitatively

very similar to that which we observe in Ge2Sb2Te5. The elipsometry analysis of Refs. 46 and 47 in the visible wavelength range showed that one hour of illumination caused significant apparent decrease of *k* at high photon energies (> 2 eV) and an increase at low photon energies, which appeared to be a red-shift of the optical bandgap. However, surface effects such as the photo-oxidation we have observed were not discussed in Refs. 46 and 47. Therefore, it is highly probable that the reported photodarkening of GexSb20-xTe80 was actually a misinterpretation of photo-oxidation.

VII. SUMMARY

The optical properties of sputtered, amorphous films of GeTe, Sb_2Te_3, and $Ge_2Sb_2Te_5$ are influenced by the presence of oxygen impurities. The absorption edges in these glasses are sometimes broader than in standard chalcogenide glasses, such as $GeSe_2$ or As_2Se_3. This result implies either that the valance band consists of highly strained bonds or that large densities of defects exist. Below the optical gap the refractive index for $Ge_2Sb_2Te_5$ is approximately 3.5.

In samples of $Ge_2Sb_2Te_5$ made with large oxygen concentrations using a hot-pressed sputtering target, there exists a large ESR signal corresponding to a defect density of ~10^{19} cm^{-3}. In samples with the lowest oxygen contamination levels (~10^{19} cm^{-3}) no ESR signal is observed, which implies that the defect density is below 10^{18} cm^{-3} in these samples. ESR signals associated with the glassy SiO_2 interface with the chalcogenide films are also observed.

Amorphous films of $Ge_2Sb_2Te_5$ can be deposited up to several μm thick by sputtering onto room temperature substrates. In these films the Ge, Sb, and Te atoms have average numbers of nearest neighbors that are approximately 4, 3, and 2.5, respectively. Consistent with a simple structural model, there exist also some Ge-Ge bonds because the measured average coordination

number for Te is less than 2.8. The films exhibit “columnar-like” voids that vary with growth rate.

$Ge_2Sb_2Te_5$ has a strong tendency to oxidize when it is illuminated by near- and above-bandgap light. Observed changes in elipsometry data obtained from thin films of Ge2Sb2Te5 under progressive illumination can be accounted for quantitatively in terms of the formation of a surface oxide layer, as confirmed by SIMS. The oxide has lower values of (*n*, *k*) than Ge2Sb2Te5, and can be etched by hydrofluoric acid or water. No change in the optical constants of the Ge2Sb2Te5 was detected even after 28 hours of illumination. Our analysis strongly suggests that previously reported observations of photodarkening in amorphous thin films of GexSb20-xTe80 are actually attributable to photo-oxidation, rather than changes in the optical constants of the GexSb20-xTe80. Our observation of negligible photodarkening in Ge2Sb2Te5 is consistent with the findings that tellurides are much less susceptible to photodarkening than selenides or sulfides, and that an increase in the mean coordination number in the alloy further reduces the photodarkening effect.

References

1. S. Hudgens and B. Johnson, MRS Bulletin, November (2004), p. 829.
2. J. D. Maimon, K. K. Hunt, L. Burcin, and J. Rodgers, IEEE Trans. Nucl. Sci. **50**, 1878 (2003); J. Maimon, K. Hunt, L. Burcin, and K. Knowles, AIP Conf. Proc. **699**, 639 (2004).
3. J. K. Olson, H. Li, and P. C. Taylor, J. Ovonic Res. **1**, 1 (2005).
4. J.Z. Liu and P. C. Taylor, Solid State Commun. **70**, 81 (1989).
5. J.Z. Liu and P. C. Taylor, J. of Non-Cryst. Solids, **114**, 25 (1989).
6. P. C. Taylor, Z. M. Saleh and J. Z. Liu, in Advances in Disordered Semiconductors, Vol. 3, H. Fritzsche, ed. (World Scientific, Singapore, 1991), p. 3.
7. N. F. Mott, Adv. in Phys. **16**, 49 (1967).
8. A. V. Kolobov, P. Fons, A. I. Frenkel, A. L. Ankudinov, J. Tominaga, and T. Uruga, Nature Materials, (2004) [on-line].
9. D. A. Baker and D. E. Sayers, unpublished.
10. K. S. Liang, A. Bienenstock, and C. W. Bates, Phys. Rev. **B10**, 1528 (1974); S. Laderman, A. Bienenstock, and K. S. Liang, Solar Energy Mat. **8**, 15 (1982), and references contained therein.
11. J. Z. Liu and P. C. Taylor, Phys. Rev. Lett. **59**, 1938 (1987).
12. B. Effey and R. L. Cappelletti, Phys. Rev. **B59**, 4119 (1999).
13. P. Boolchand and W. J. Bresser, Philos. Mag. **B80**, 1757 (2000).
14. N. M. Amer and W. B. Jackson, in *Semiconductors and Semimetals*, Vol. 21B, J. I. Pankove, ed. (Academic Press, N.Y., 1984,), p. 83; W. B. Jackson and N. M. Amer, Phys. Rev. **B25**, R5559 (1982).

15. B. Yan, N. A. Schultz, A. L. Efros, and P. C. Taylor, Phys. Rev. Lett. **84**, 4180 (2000); B. Yan and P. C. Taylor, MRS Symp. Proc. **507**, 787 (1998).

16. S.G. Bishop, U. Strom, and P. C. Taylor, Phys. Rev. **B15**, 2278 (1977).

17. P. W. Atkins and M. C. R. Symons, *The Structure of Inorganic Radicals* (Elsevier, Amsterdam, 1967), p. 21.

18. G. W. Charles, J. Opt. Soc. Amer. **58**, 275 1968).

19. P. C. Taylor, H.M. Kriz and J. F. Baugher, Chemical Reviews **75**, 203 (1975).

20. D. L. Griscom, in *Glass Science and Technology*, Vol. 4B (Elsevier, Amsterdam, 1992), p. 151.

21. A. Morimoto, T. Miura, M. Kumeda, and T. Shimizu, Jpn. J. Appl. Phys. **20**, L833 (1981).

22. I. Watanabe, M. Ishikawa, and T. Shimizu, J. Phys. Soc. Jpn. **45**, 1603 (1978).

23. P. C. Taylor, in *The Physics of Non-Crystalline Solids* (Taylor and Francis, London, 1972), p. 731.

24. See, for example, T. Su, P. C. Taylor, and J. Whitaker, MRS Symp. Proc. **808**, 141 (2004).

25. L. Tichy, A. Triska, M. Frumar, H. Ticha, and J. Klikorka, J. Non-Cryst. Solids **50**, 371 (1982).

26. A. M. El-Korashy, Egypt. J. Solids **7**, 13 (1985).

27. A. M. El-Korashy, Phys. Status Solidi **B146**, 279 (1988).

28. S. K. Bahl and K. L. Chopra, J. Appl. Phys. **41**, 2196 (1970).

29. S. D. Shutov, V. V. Sobolev, Y. V. Popov, and S. N. Shestatskii, Phys. Stat. Solidi **31**, K23 (1969).

30. T. Aoki, H. Shimada, N. Hirao, N. Yoshida, K. Shimakawa, and S. R. Elliott, Phys. Rev. **B59**, 1579 (1999).

31. A. L. Jung, H. Situ, Y. W. Lu, Z. T. Wang, and Z. G. He, J. Non-Cryst. Solids **114**, 55 (1989).

32. W. Procarione and C. Wood, Phys. Stat. Solidi **42**, 871 (1970).

33. A. Von Middendorf, K. Dietrich, and G. Lanwehr, Solid State Commun. **13**, 443 (1973).

34. E. Morales-Sanchez, E. F. Prokhorov, A. Mendoza-Galvin, and J. Gonzalez-Hernandez, **69**, 361 (2003).

35. N. F. Mott and E. A. Davis, *Electronic Processes in Non-Crystalline Materials* (Clarendon Press, Oxford, 1979).

36. K. Weiser and M. H. Brodsky, Phys. Rev. **B1**, 791 (1970).

37. R. H. Bube, J. F. Mahan, R. T.-S. Shiah, and H. A. Vander Plas, Appl. Phys. Lett. **25**, 419 (1974); C. M. Garner, L. R. Gilbert, and C. Wood, J. Non-Cryst. Solids **15**, 63 (1974).

38. P. C. Taylor, E. J. Friebele, and S. G. Bishop, Solid State Commun. **28**, 247 (1978).

39. H. Scher and E. W. Montroll, Phys. Rev. **B12**, 2455 (1975); G. Pfister and H. Scher, Phys. Rev. **B15**, 2062 (1977).

40. D. Emin, Adv. Phys. **24**, 305 (1975).

41. D. A. Baker, S. C. Agarwal, G. Lucovsky, M. A. Paesler, and P. C. Taylor, MRS Symp. Proc. **918**, 157 (2006).

42. D. A. Baker, S. C. Agarwal, G. Lucovsky, M. A. Paesler, and P. C. Taylor, J. Non-Cryst. Solids **352**, 1621 (2006).

43. B.-S. Lee, Y. Xiao, S. G. Bishop, J. R. Abelson, S. Raoux, V. R. Deline, M.-H. Kwon, K.-B. Kim, B.-K. Cheong, and P. C. Taylor, MRS Symp. Proc. **918**, 113 (2006).

44. B.-S. Lee, J. R. Abelson, S. G. Bishop, D. H. Kang, B. K. Cheong, and K. B. Kim, *J. Appl. Phys.* **97,** 093509 (2005).

45. K. Shimakawa, A. Kolobov, and S. R. Elliott, *Adv. Phys.* **44,** 475-588 (1995).

46. V. Pamukchieva, A. Szekeres, and K. Todorova, *Proceedings of SPIE-The International Society for Optical Engineering* **5581,** 608-13 (2004).

47. V. Pamukchieva and A. Szekeres, *J. Optoelec. Adv. Mater.* **7,** 1277-80 (2005).

Table I. Dependence of oxygen concentration on growth rate in Ge-Sb-Te sputtered films.

Sample ID	*Composition*	*Growth Rate (Å/s)*	*Oxygen Concentration*	*Notes*
106, 130, 138	$Ge_2Sb_2Te_5$	6	$5x10^{20}$ - 10^{22} cm^{-3}	Pressed Target
225	$Ge_2Sb_2Te_5$	6	$1x10^{19}$ cm^{-3}	
268	$Ge_2Sb_2Te_5$	3	$3x10^{19}$ cm^{-3}	
276	$Ge_2Sb_2Te_5$	1.5	$3x10^{20}$ cm^{-3}	
286	$Ge_2Sb_2Te_5$	0.75	$1x10^{21}$ cm^{-3}	
220	Sb_2Te_3	6	$3x10^{20}$ cm^{-3}	
260	Sb_2Te_3	3	$2x10^{20}$ cm^{-3}	
310	Sb_2Te_3	1.5	$4x10^{20}$ cm^{-3}	
325	Sb_2Te_3	0.75	$4x10^{20}$ cm^{-3}	
234	GeTe	6	$1x10^{20}$ cm^{-3}	
252	GeTe	3	$3x10^{20}$ cm^{-3}	
294	GeTe	1.5	$1x10^{21}$ cm^{-3}	
302	GeTe	0.75	$3x10^{21}$ cm^{-3}	

Table II. Optical band gaps in Ge-Sb-Te crystals and glasses.

Compound	Crystal Band Gap (eV)	Amorphous Band Gap (eV)	Ref.
GeS	1.6	1.4	25,26
GeSe	1.0		27
GeTe	0.2	0.8	28
		0.85	present work
Sb_2S_3	1.7	1.7	25,29
Sb_2Se_3	1.2	1.25	29,30
Sb_2Te_3	0.15-0.2	0.55-0.8	29,31-33
		0.45	present work
$Ge_2Sb_2Te_5$	0.2		34
		0.85	present work
As_2S_3		2.4	35
As_2Se_3		1.8	35
As_2Te_3		0.95	36

Figure Captions

Fig. 1 Ternary composition diagram for the system Ge-Sb-Te. Open diamonds indicate specific compositions along pseudo-binary tie lines. The dotted line represents those compositions for which there exist only Ge-Te and Sb-Te bonds if the Te remains two-fold coordinated. The dashed line represents those compositions whose average coordination numbers are constant (if the Te remains two-fold coordinated) at 2.67. The solid line includes the compositions most often used for phase-change memory applications.

Fig. 2 SIMS profile for a film of amorphous $Ge_2Sb_2Te_5$ grown using a cast target at 6 Å/s.

Fig. 3 Optical absorption coefficients in amorphous films of GeTe (dotted line), Sb_2Te_3 (dashed line), and $Ge_2Sb_2Te_5$ (solid line) measured by PDS. Films were grown at 6 Å/s using cast targets.

Fig. 4 Optical absorption in a series of amorphous films of $Ge_2Sb_2Te_5$. Solid line (with highest absorption) was grown at 6 Å/s using the cast target; dotted line was grown at 6 Å/s using the hot-pressed target; short dashed line was grown at 3 Å/s using the cast target; long dashed line was grown at 1.5 Å/s using the cast target; solid line (lowest absorption) was grown at 0.75 Å/s using the cast target. All films were approximately one to two μm thick.

Fig. 5 Optical absorption in a series of amorphous films of GeTe. Solid line was grown at 6 Å/s using the hot-pressed target; dotted line was grown at 6 Å/s using the cast target; dashed line was grown at 3 Å/s using the cast target. The indices of refraction below the gap for the solid and dashed lines are approximately 4.5 and 4.9, respectively. All films were approximately one to two μm thick.

Fig. 6 Energy at which the absorption coefficient is 10^4 cm^{-1} (E_{04}, filled symbols) as a function of oxygen concentration. Inverse slope of the exponential component of the optical absorption (ΔE, open symbols) as a function of oxygen concentration. Circles denote data for amorphous $Ge_2Sb_2Te_5$, and squares denote data for amorphous GeTe.

Fig. 7 Real part of the index of refraction as a function of oxygen concentration in amorphous films of $Ge_2Sb_2Te_5$. Filled circles and triangle are samples grown using the cast and hot-pressed targets, respectively. Note: The samples shown in this figure are not the same as those listed in Table I.

Fig. 8 ESR spectrum of amorphous $Ge_2Sb_2Te_5$ grown at 6 Å/s using the hot-pressed target. The solid line is a simulation of the spectrum assuming the same hybridized wave function as for paramagnetic centers on sulfur and selenium but scaled by the strength of the spin-orbit coupling constant. The spectrometer operating parameters are different from those employed for the spectra in Fig. 9.

Fig. 9 ESR spectra of amorphous $Ge_2Sb_2Te_5$. Top spectrum is for a sample grown at 3 Å/s using a cast target; middle spectrum is for a sample grown at 6 Å/s using a cast target; bottom spectrum is for a sample grown at 6 Å/s using a hot-pressed target. The spectrometer operating parameters are different from those employed for the spectra in Fig. 8.

Fig. 10 ESR spectra of amorphous films deposited from a cast source. (a) $Ge_2Sb_2Te_5$ (top trace) grown at 3 Å/s; (b) Sb_2Te_3 grown at 6 Å/s; (c) GeTe grown at 6 Å/s; (d) simulation of the spectra in (a) through (c) assuming equal densities of an e' (electron) center and an oxygen (hole) center as observed in oxide glasses. The spectrometer operating parameters are different from those employed for the spectra in Fig. 8.

Fig. 11 ESR intensity for the interface-related spectra of the type shown in Fig. 10 for amorphous $Ge_2Sb_2Te_5$ as a function of oxygen concentration. Solid circles and the square are data for samples made using cast and hot-pressed targets, respectively.

Fig. 12 ESR spectra for amorphous $Ge_2Sb_2Te_5$ grown at 6 Å/s. The top and bottom spectra were grown using cast and hot-pressed targets, respectively. For the top spectrum the vertical scale has been expanded by a factor of 60. A comparison of these two spectra provides an upper bound for the density of the ESR center associated with Te in the samples made with the cast target.

Fig. 13 Inverse slope of the exponential band-tail absorption (ΔE) in amorphous $Ge_2Sb_2Te_5$ as a function of growth rate. Solid circles and square are data for samples made with cast and hot pressed targets, respectively.

Fig. 14 AFM image of amorphous Ge2Sb2Te5 (lighter colored, wider strips) and optically crystallized Ge2Sb2Te5 (darker colored, narrower strips). See text for details.

Fig. 15 Small angle x-ray scattering data for two amorphous film of $Ge_2Sb_2Te_5$. Samples numbered 401 and 402 were grown at 6 and 3 Å/s, respectively.

Fig. 16 Small angle x-ray scattering data for an amorphous film of $Ge_2Sb_2Te_5$ grown at 6 Å/s. The differences between the scattering for the x-ray beam incident parallel to the normal to the surface of the film (0^o tilt) and that incident 45^o from the normal indicate the presence of non-spherical voids as discussed in the text.

Fig. 17 Oxygen profile before and after illumination, obtained by SIMS. Light illumination significantly accelerates the incorporation of oxygen into the film.

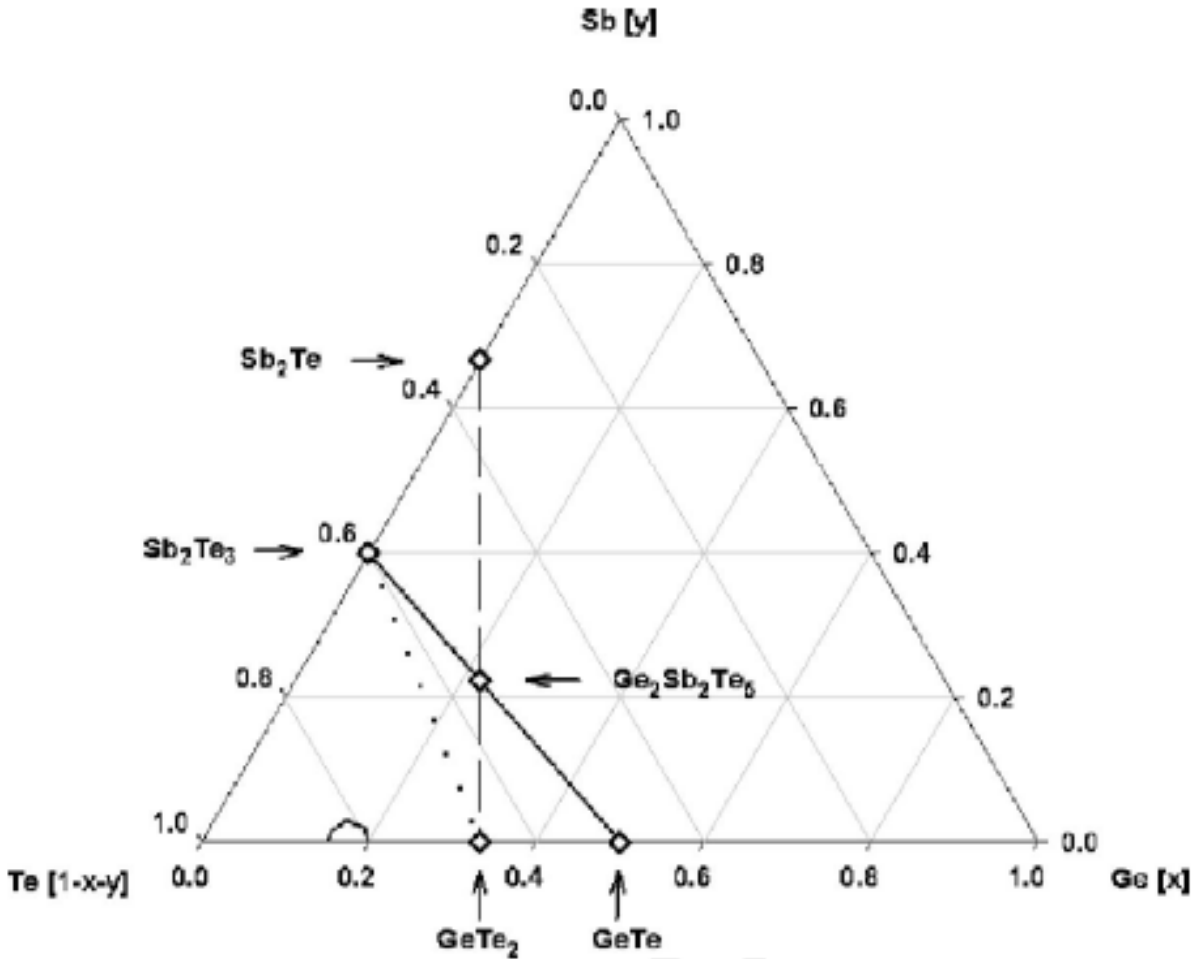
Sb [y]
0.0
1.0
0.2
0.8
Sb2Te
0.4
0.6
Sb2Te3
0.6
0.4
Ge2Sb2Te5
0.8
0.2
1.0
0.0
Te [1-x-y]
0.0
0.2
0.4
0.6
0.8
1.0
Ge [x]
GeTe2
GeTe

Figure 1

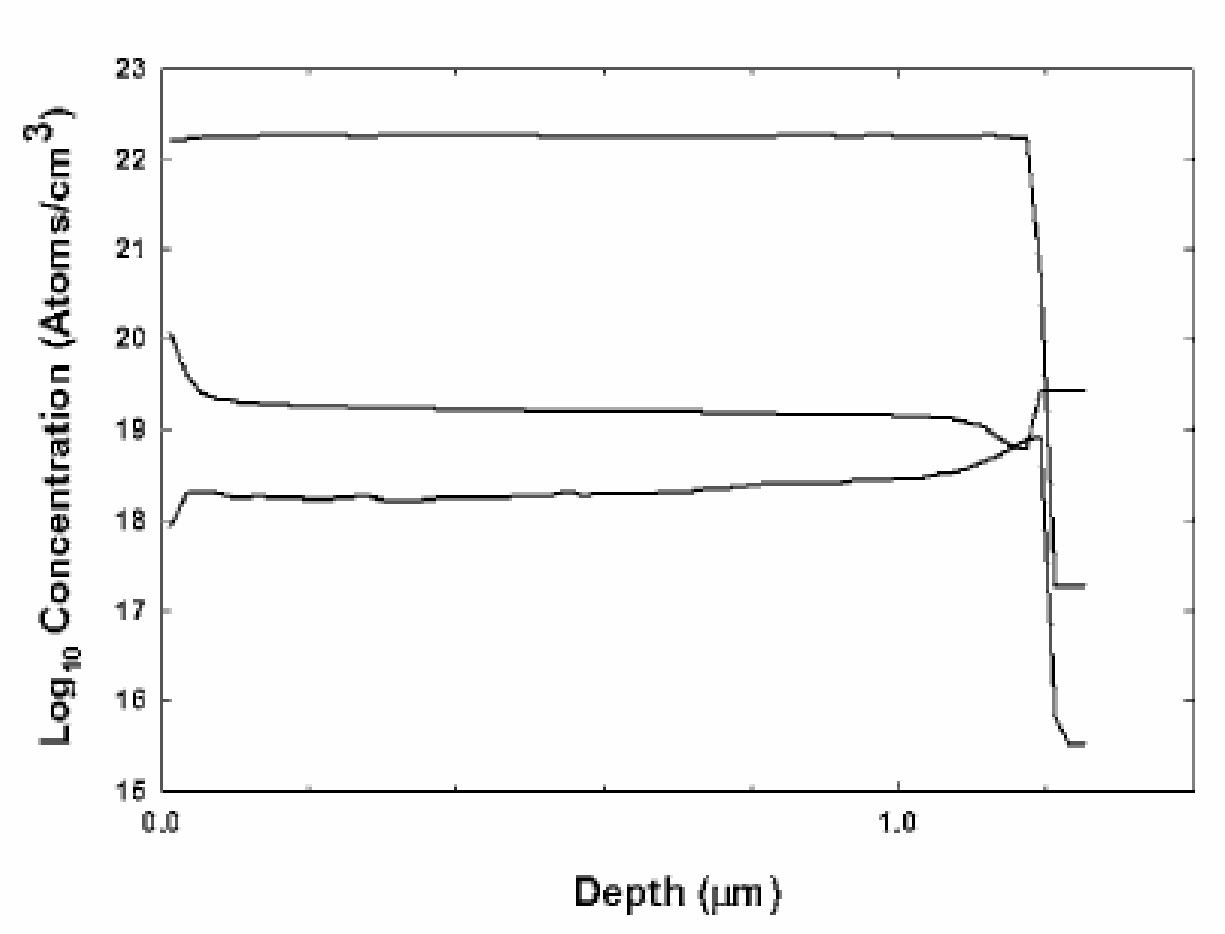
23
22
21
20
19
18
17
16
15
0.0
1.0
Log10 Concentration (Atoms/cm3)
Depth (μm)

Figure 2

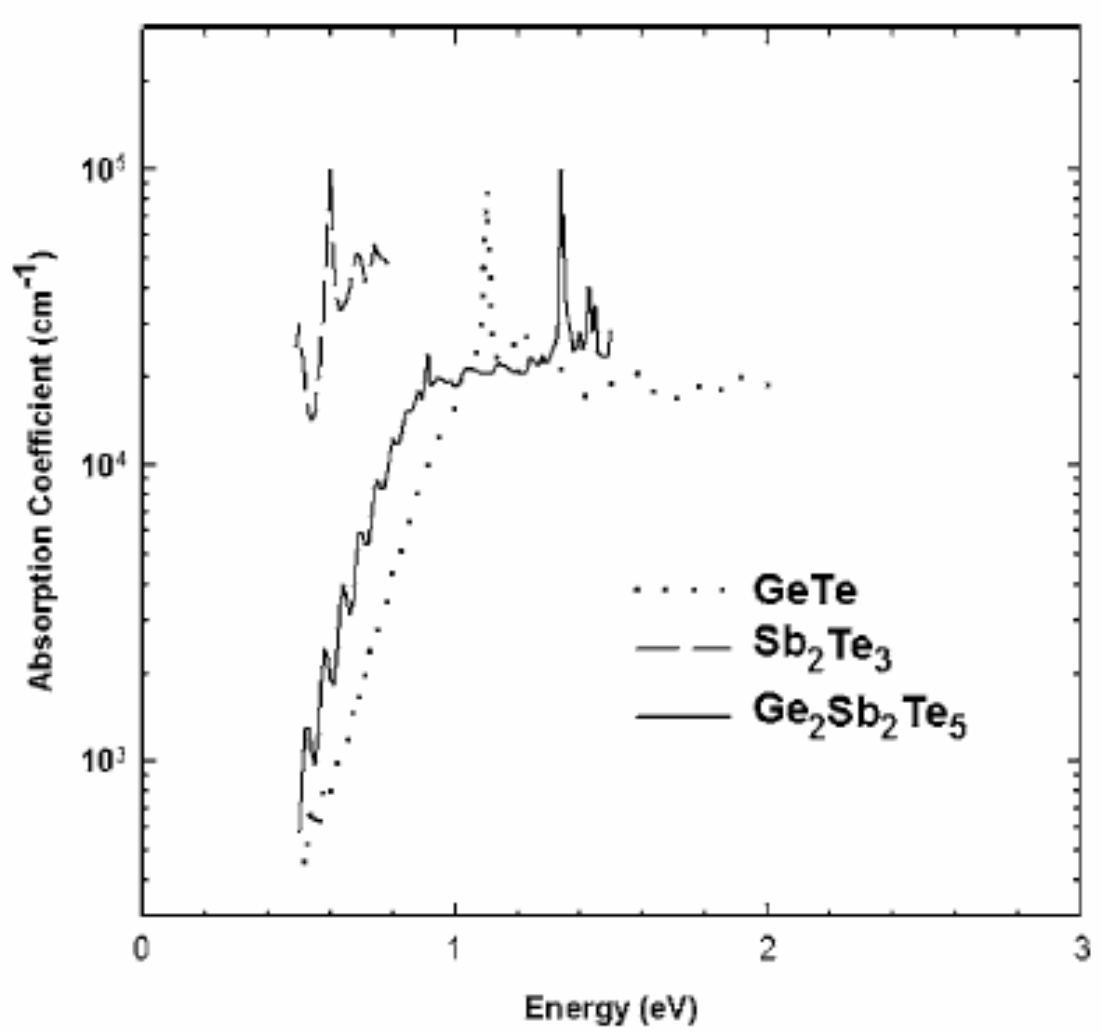
Absorption Coefficient (cm^{-1})
10^5
10^4
10^3
0
1
2
3
Energy (eV)
GeTe
Sb_2Te_3
$Ge_2Sb_2Te_5$

Figure 3

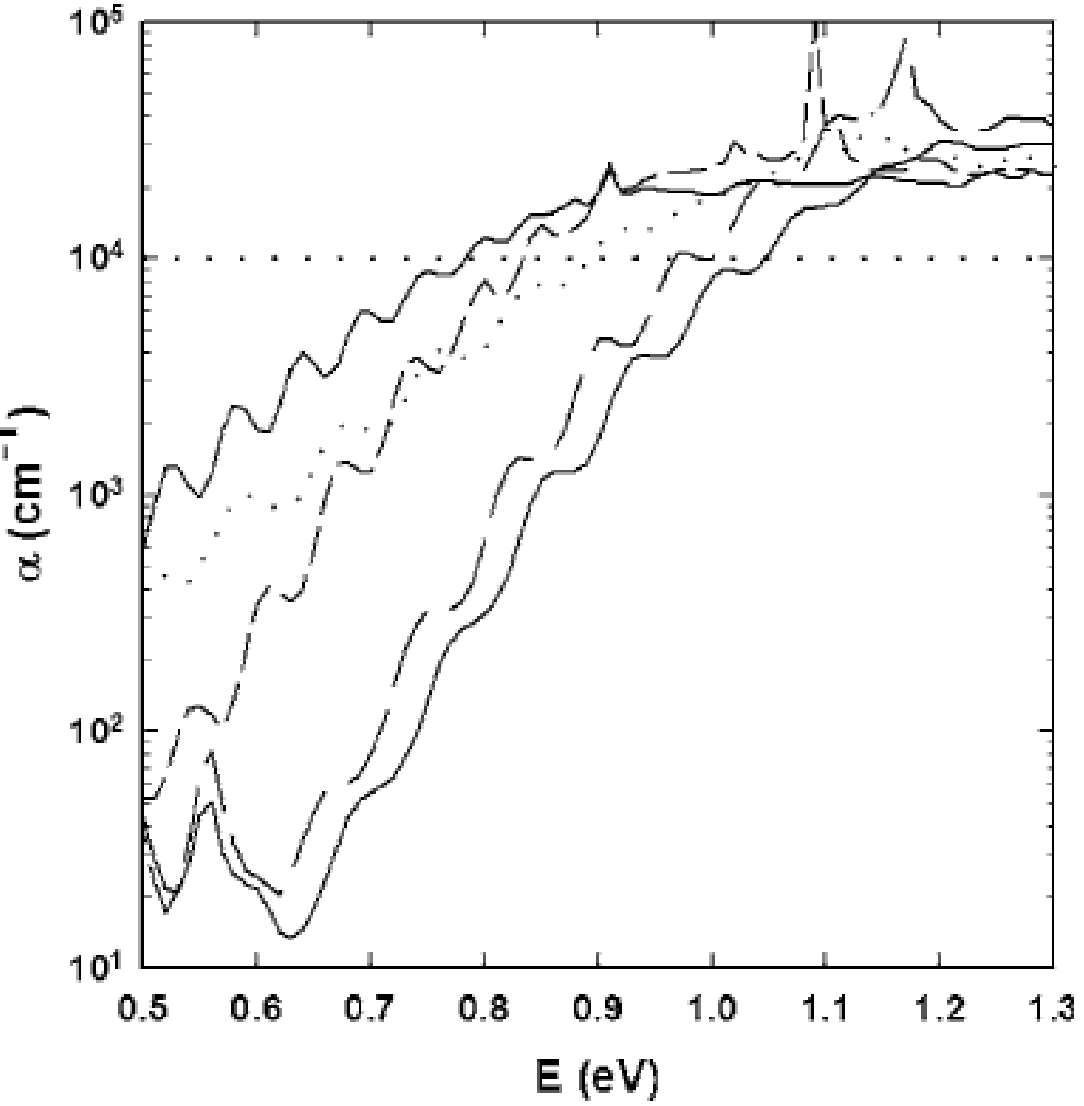

Figure 4

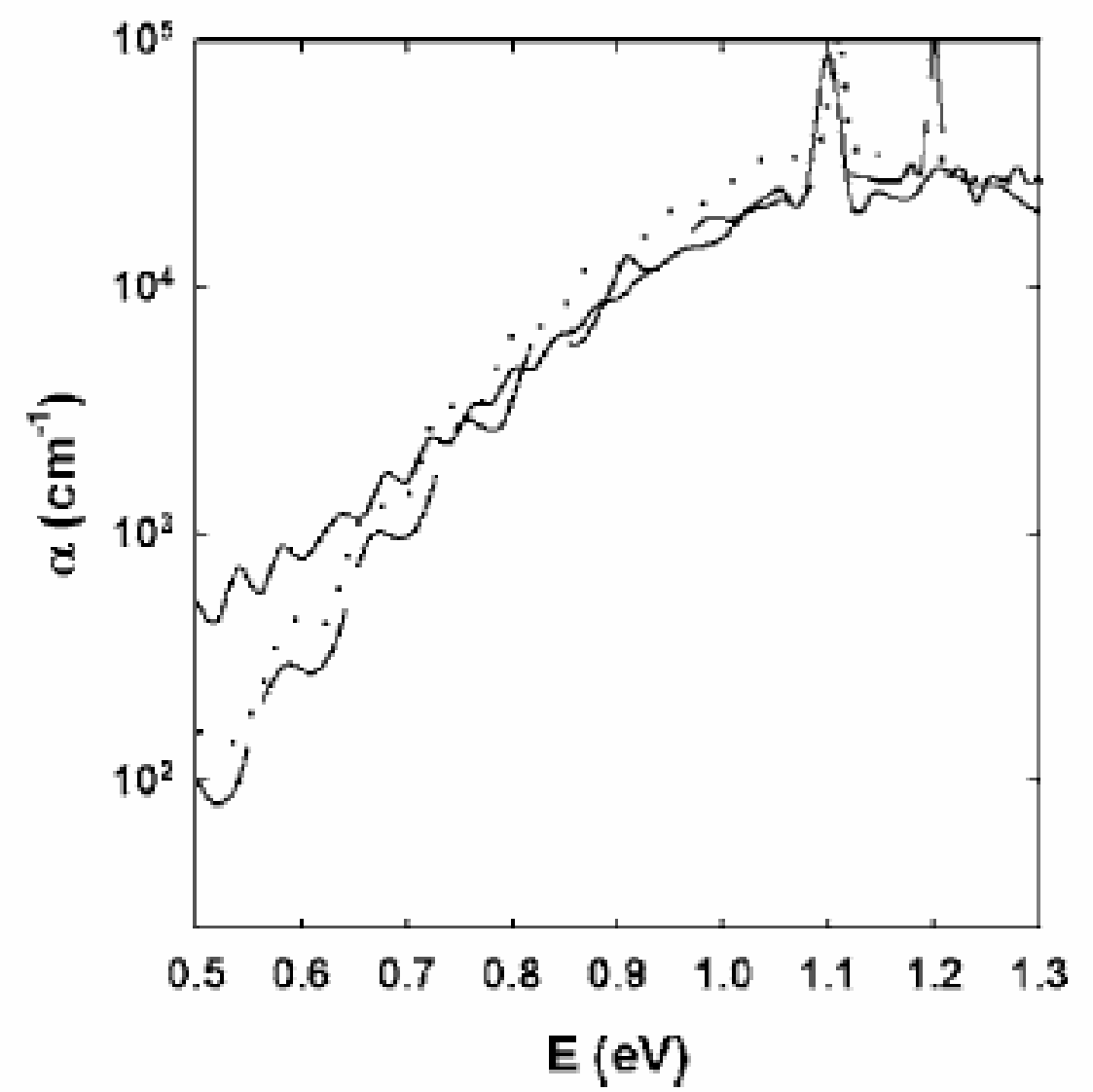

Figure 5

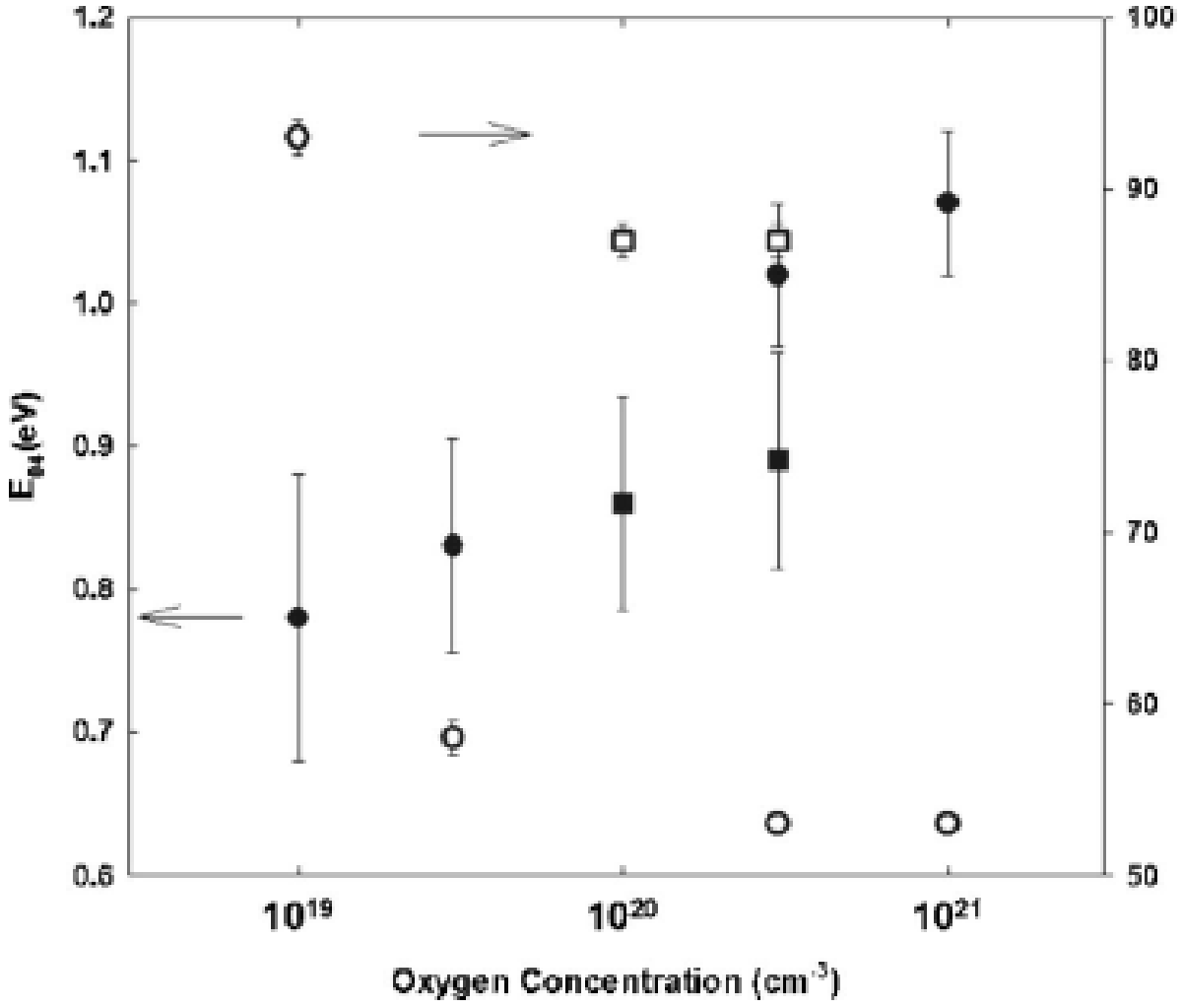
1.2
1.1
1.0
0.9
0.8
0.7
0.6
100
90
80
70
60
50
E_{act}(eV)
10^{19}
10^{20}
10^{21}
Oxygen Concentration (cm^{-3})

Figure 6

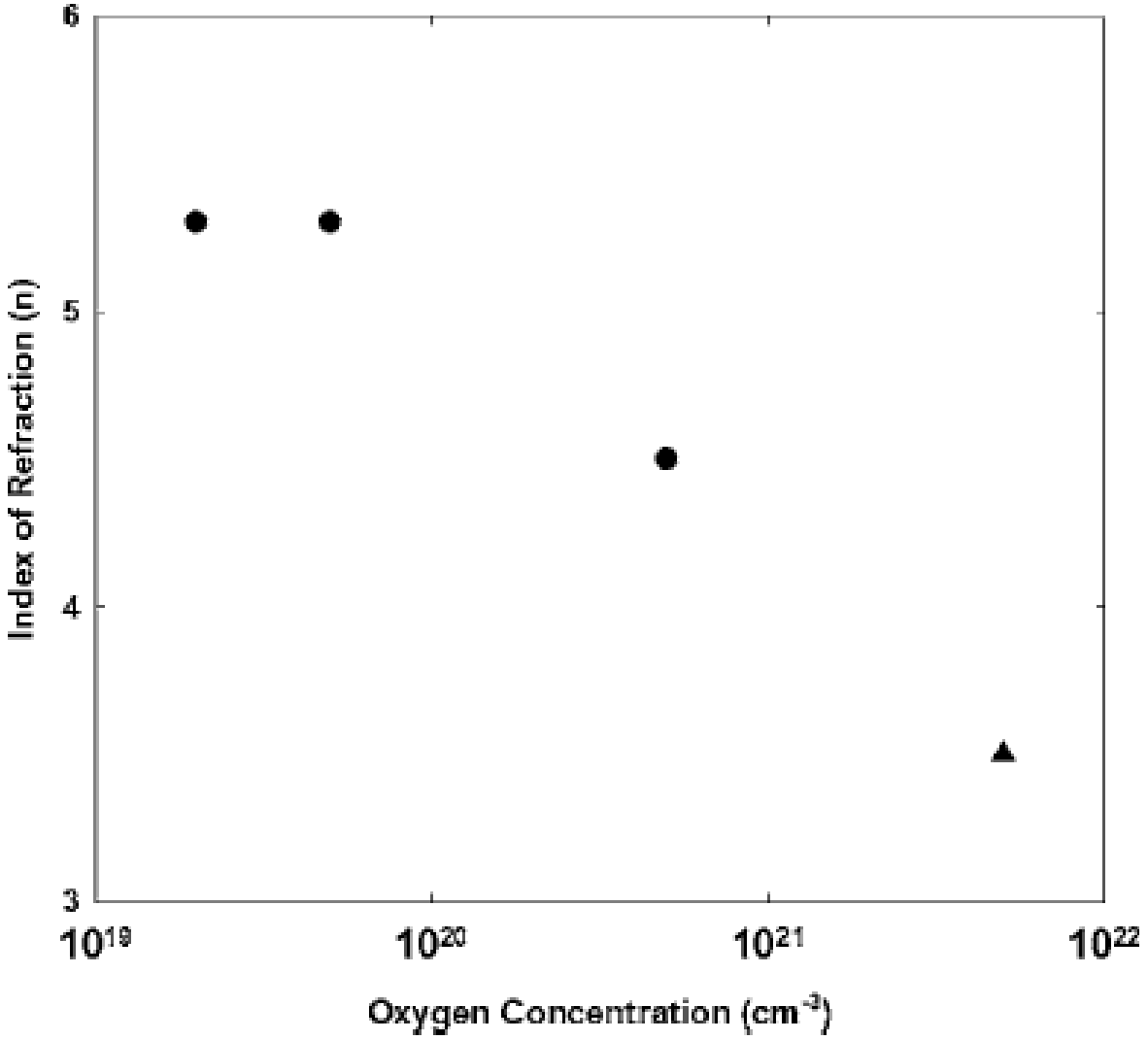
6
5
4
3
Index of Refraction (n)
10^19
10^20
10^21
10^22
Oxygen Concentration (cm^-3)

Figure 7

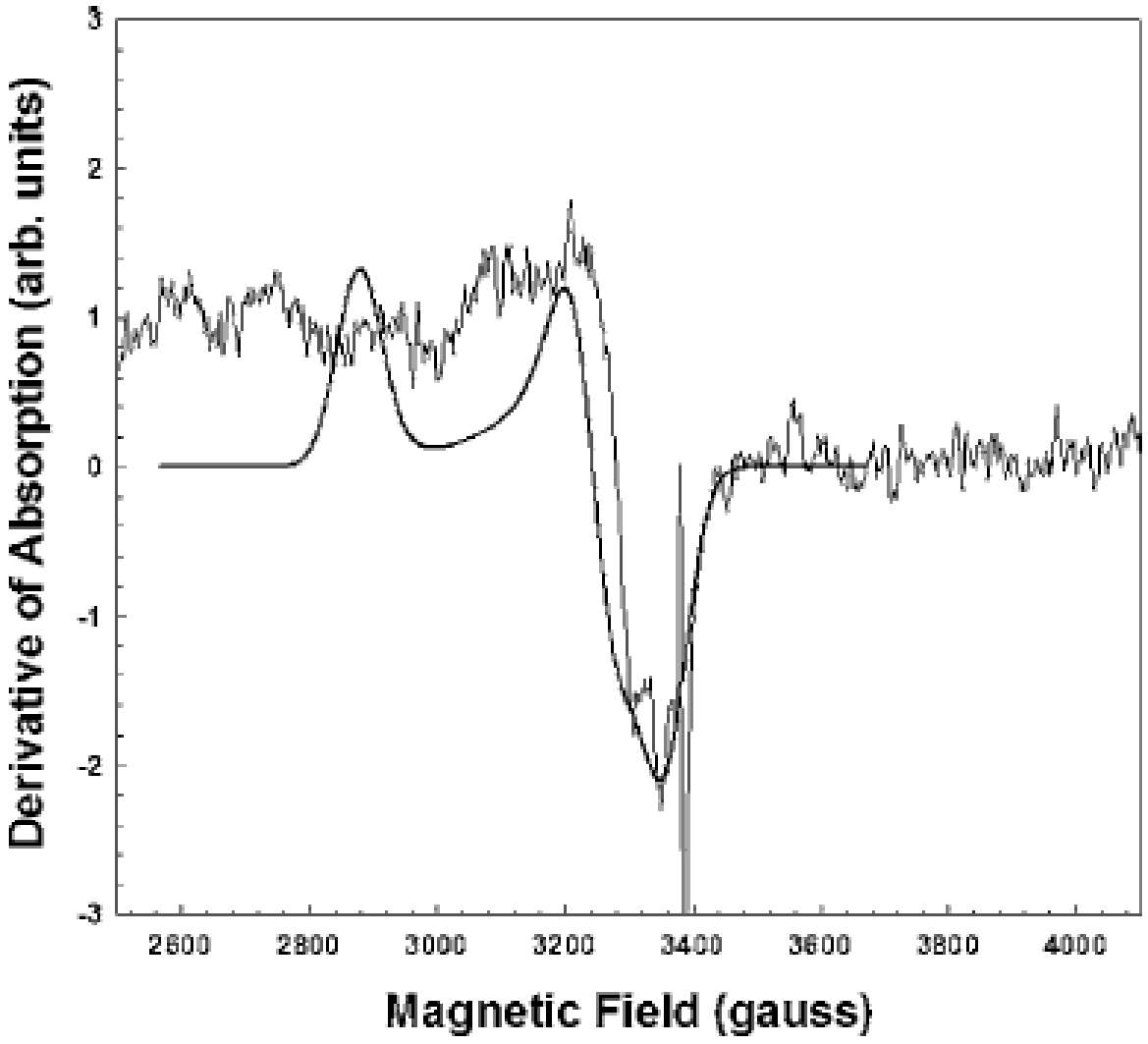
Derivative of Absorption (arb. units)
3
2
1
0
-1
-2
-3
2600
2800
3000
3200
3400
3600
3800
4000
Magnetic Field (gauss)

Figure 8

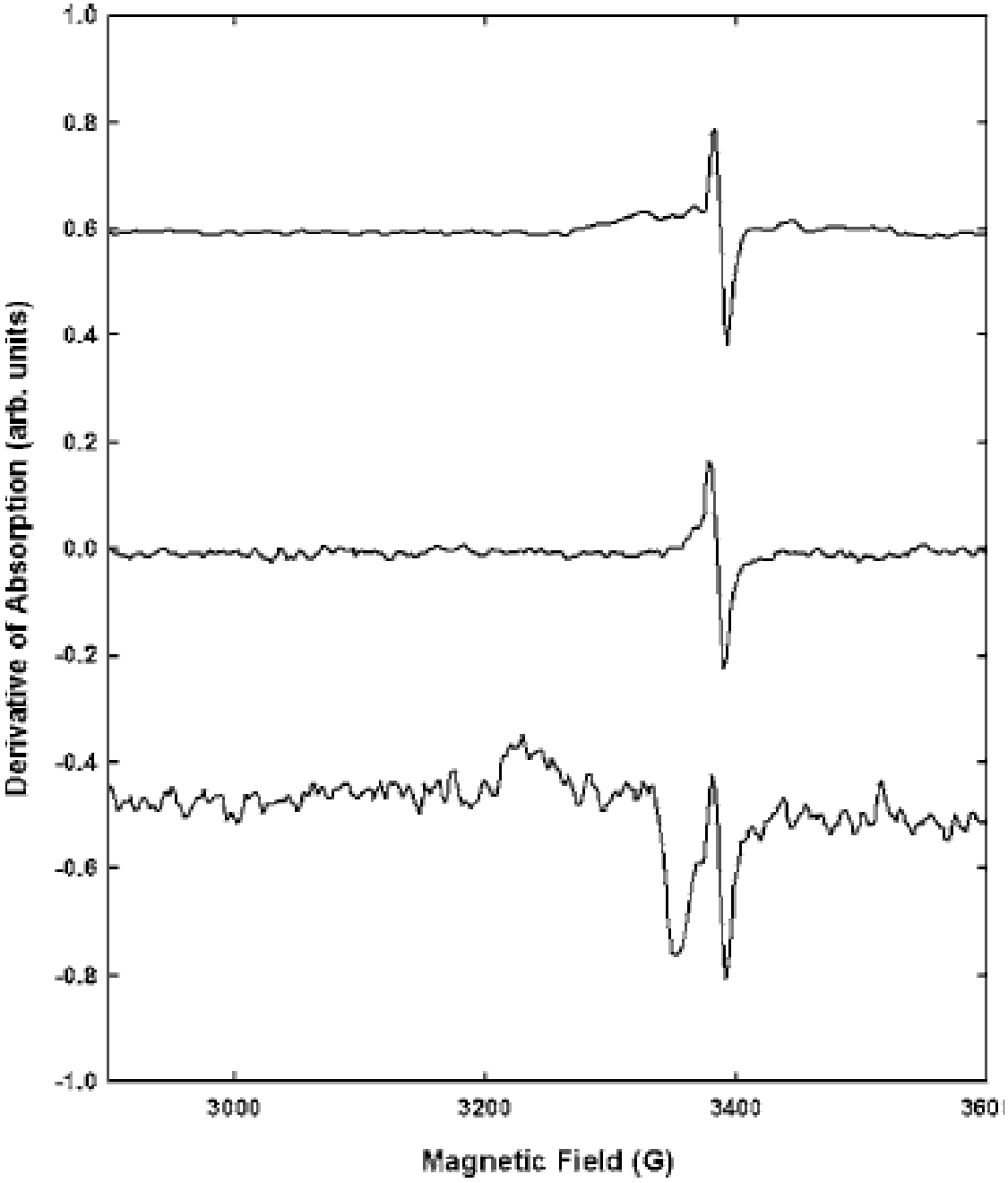
1.0
0.8
0.6
0.4
0.2
0.0
-0.2
-0.4
-0.6
-0.8
-1.0
Derivative of Absorption (arb. units)
3000
3200
3400
360
Magnetic Field (G)

Figure 9

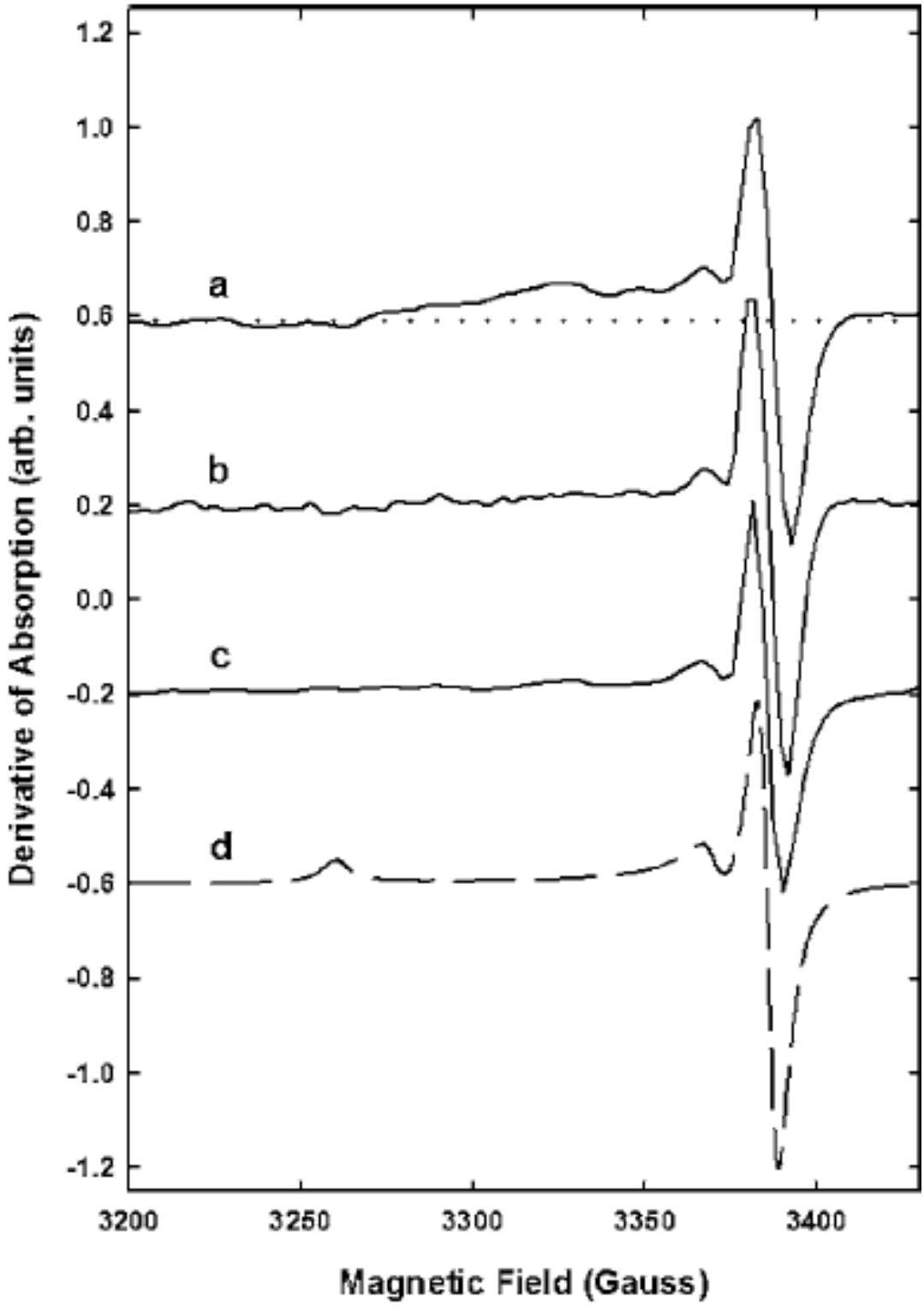
Derivative of Absorption (arb. units)
1.2
1.0
0.8
0.6
0.4
0.2
0.0
-0.2
-0.4
-0.6
-0.8
-1.0
-1.2
a
b
c
d
3200
3250
3300
3350
3400
Magnetic Field (Gauss)

Figure 10

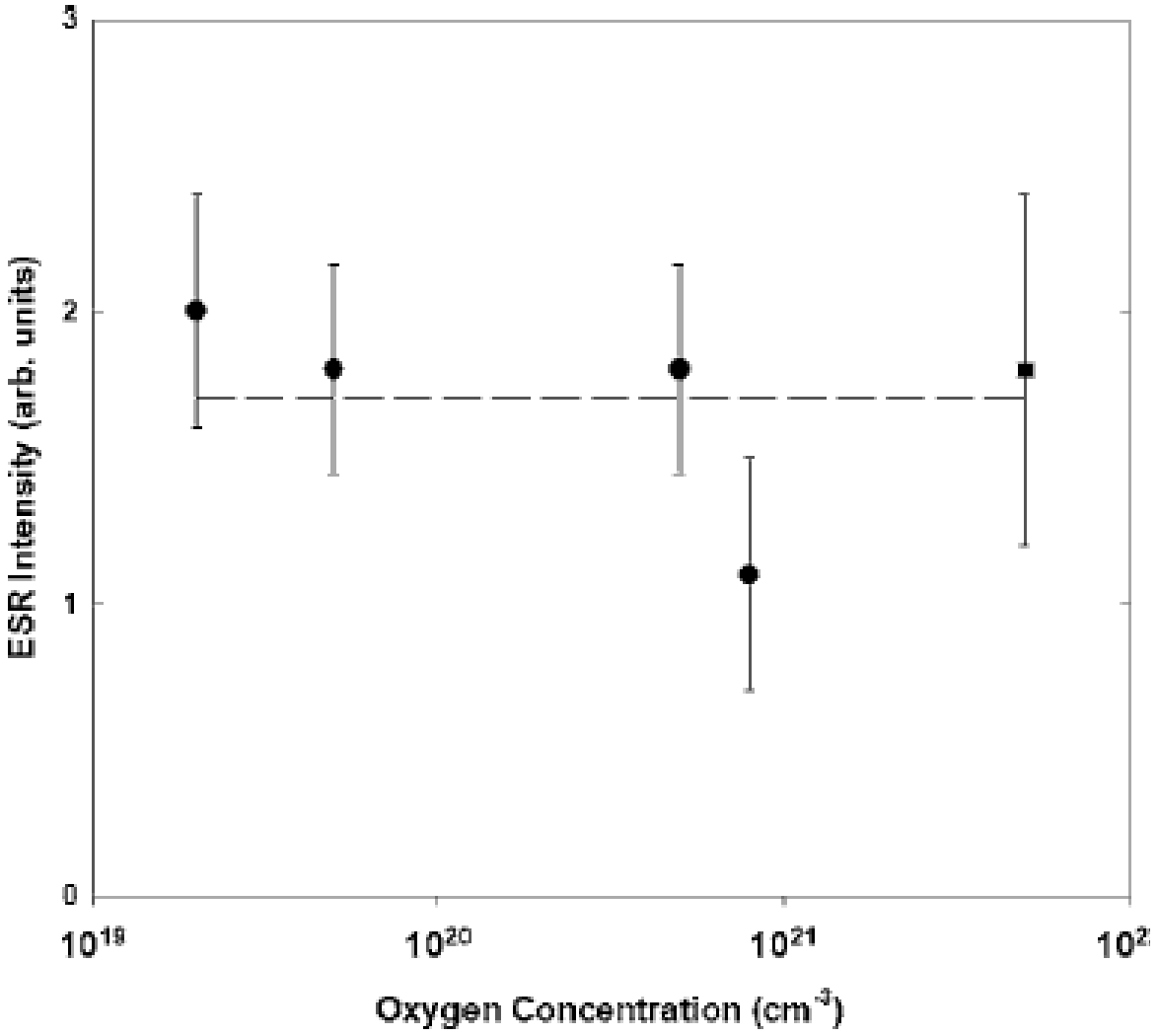
ESR Intensity (arb. units)
3
2
1
0
10^19
10^20
10^21
Oxygen Concentration (cm^-3)

Figure 11

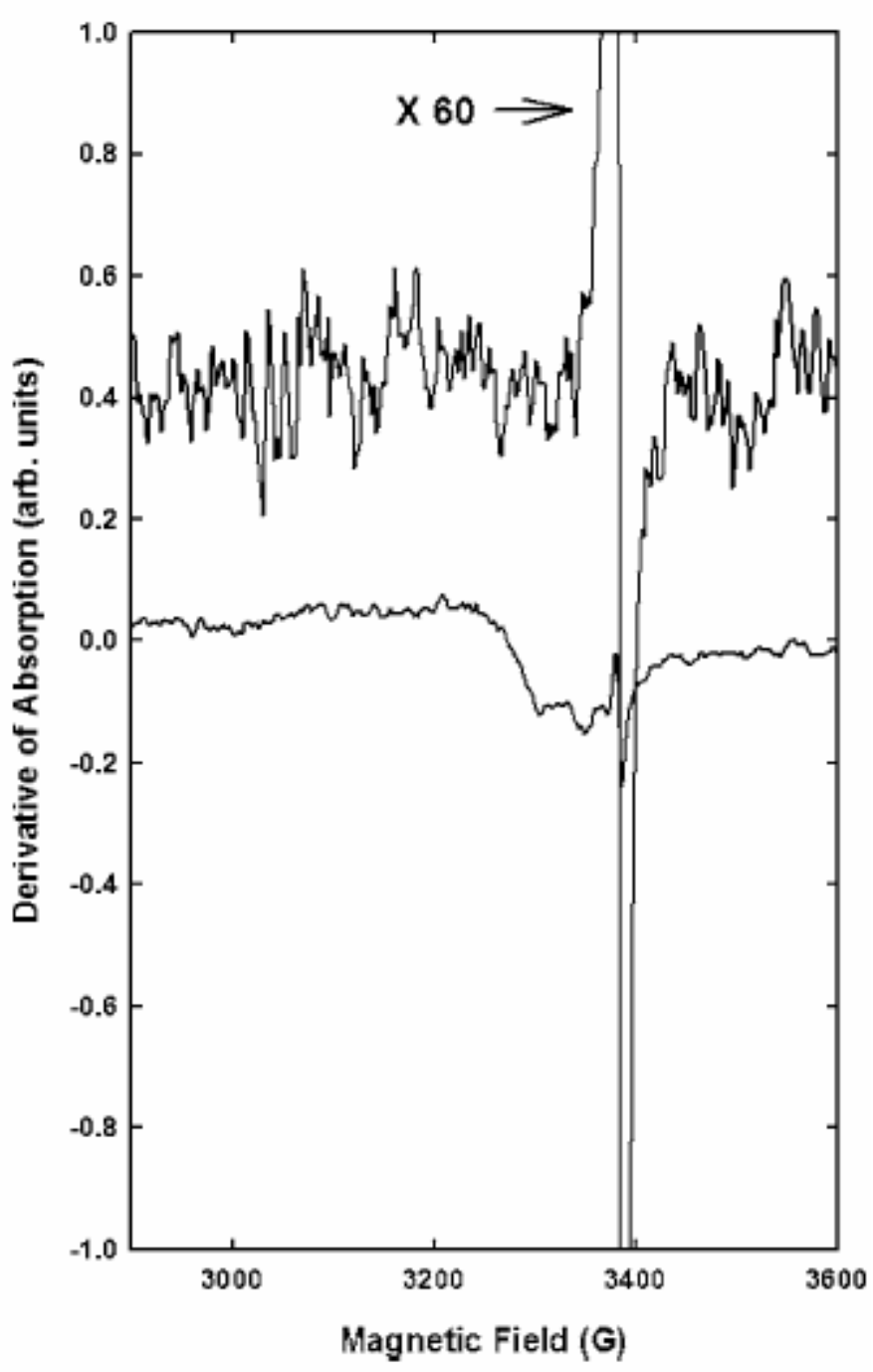
X 60
Derivative of Absorption (arb. units)
Magnetic Field (G)
1.0
0.8
0.6
0.4
0.2
0.0
-0.2
-0.4
-0.6
-0.8
-1.0
3000
3200
3400
3600

Figure 12

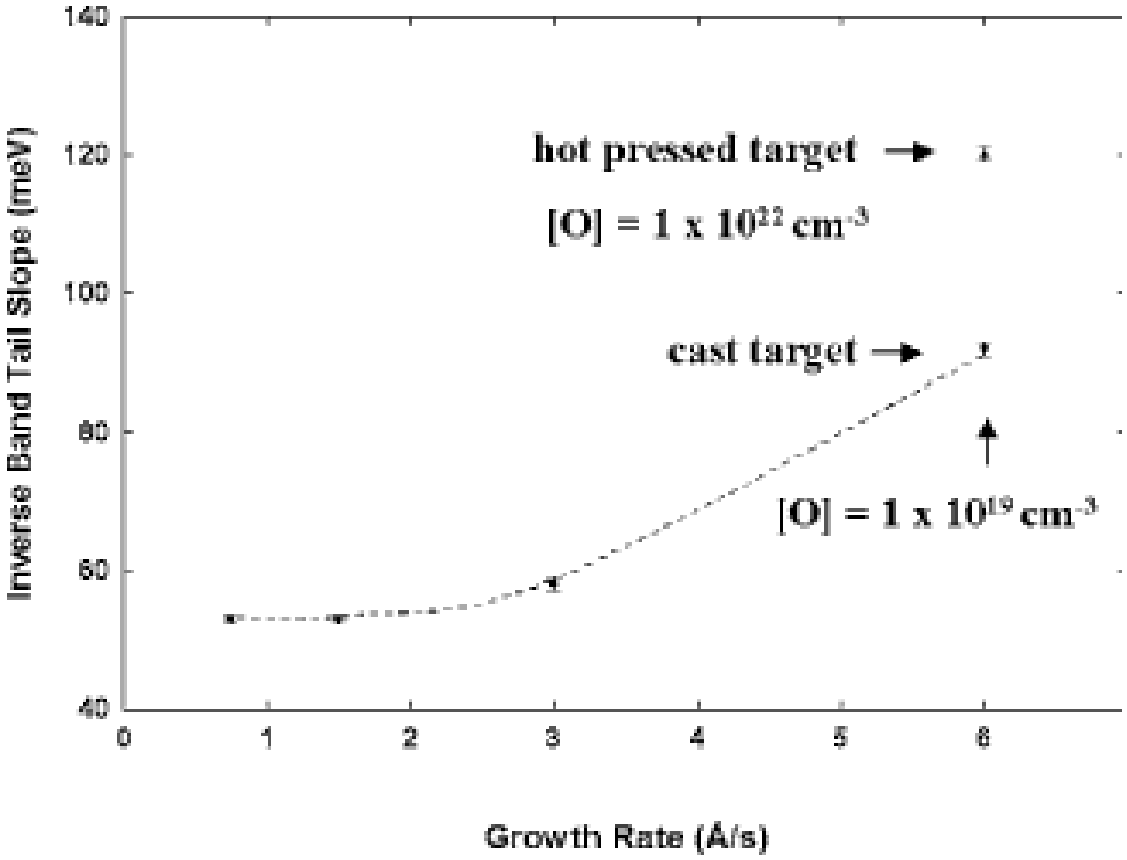
Inverse Band Tail Slope (meV)
140
120
100
80
60
40
0
1
2
3
4
5
6
Growth Rate (Å/s)
hot pressed target
[O] = 1 x 10^22 cm^-3
cast target
[O] = 1 x 10^19 cm^-3

Figure 13

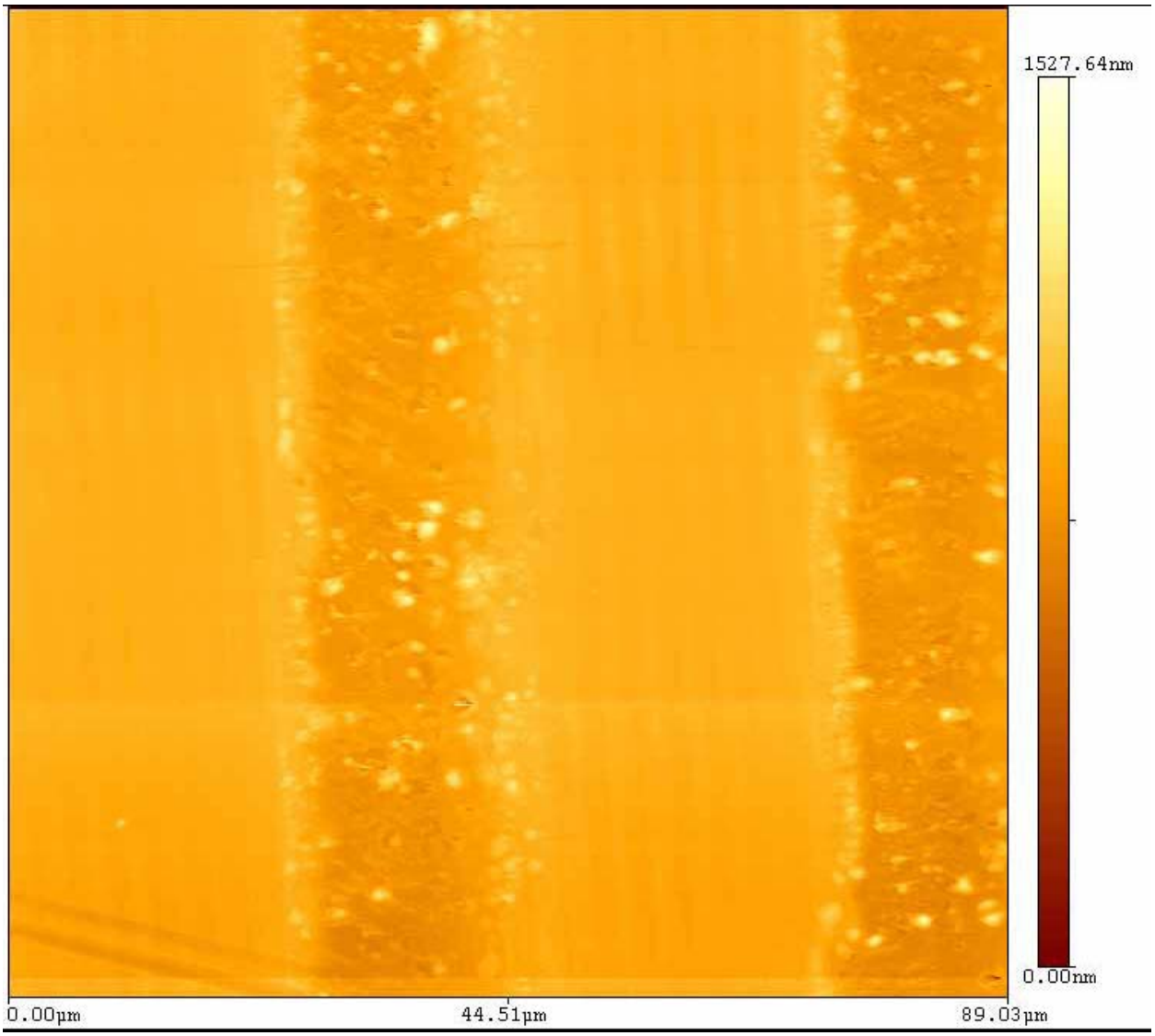

Figure 14

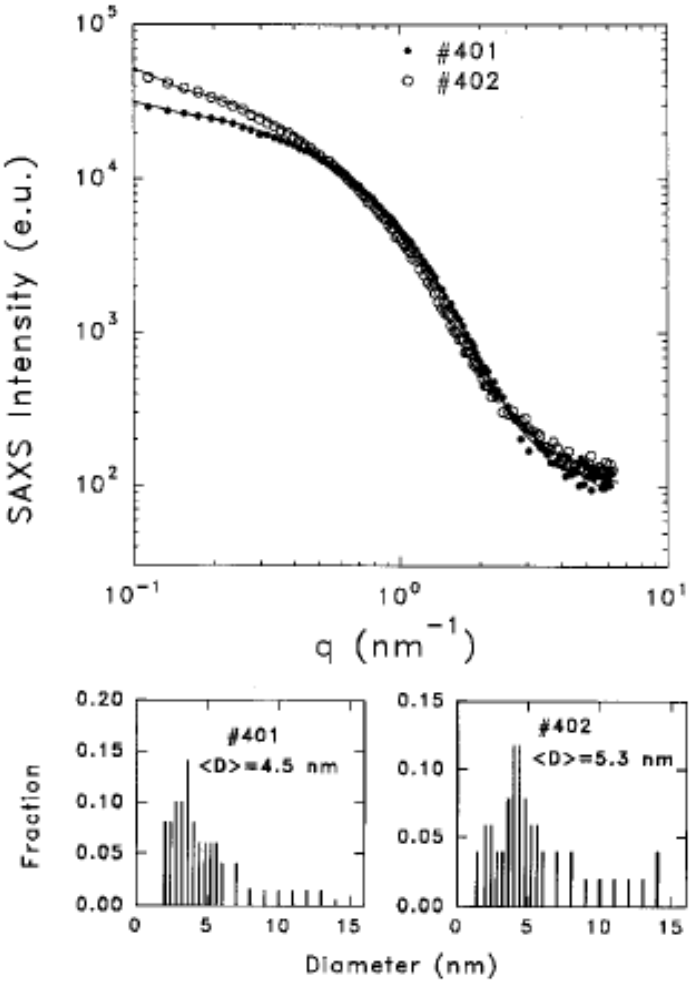
SAXS Intensity (e.u.)
q (nm^{-1})
#401
#402
Fraction
#401
<D>=4.5 nm
#402
<D>=5.3 nm
Diameter (nm)

Figure 15

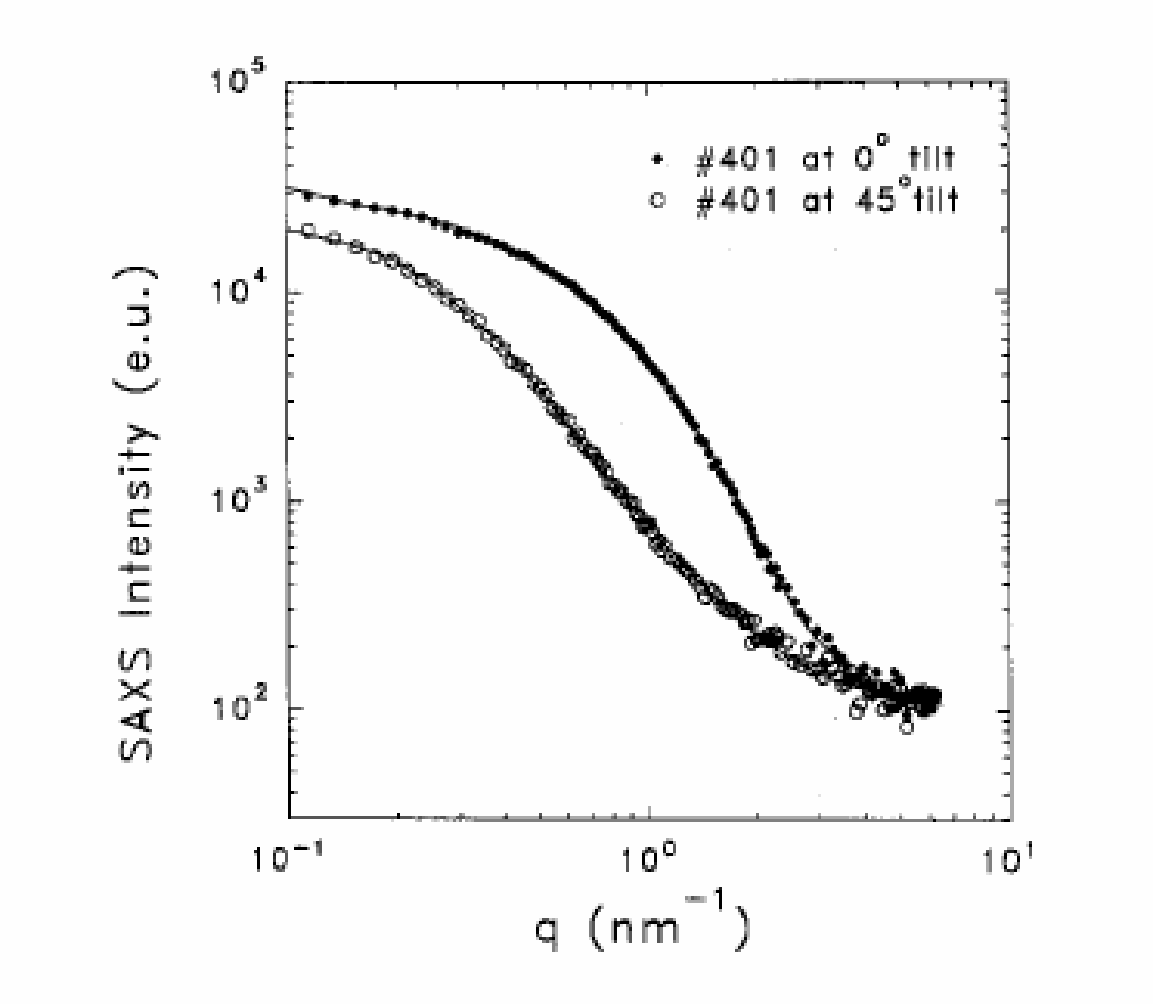
#401 at 0° tilt
#401 at 45° tilt
SAXS Intensity (e.u.)
q (nm⁻¹)
10⁵
10⁴
10³
10²
10⁻¹
10⁰
10¹

Figure 16

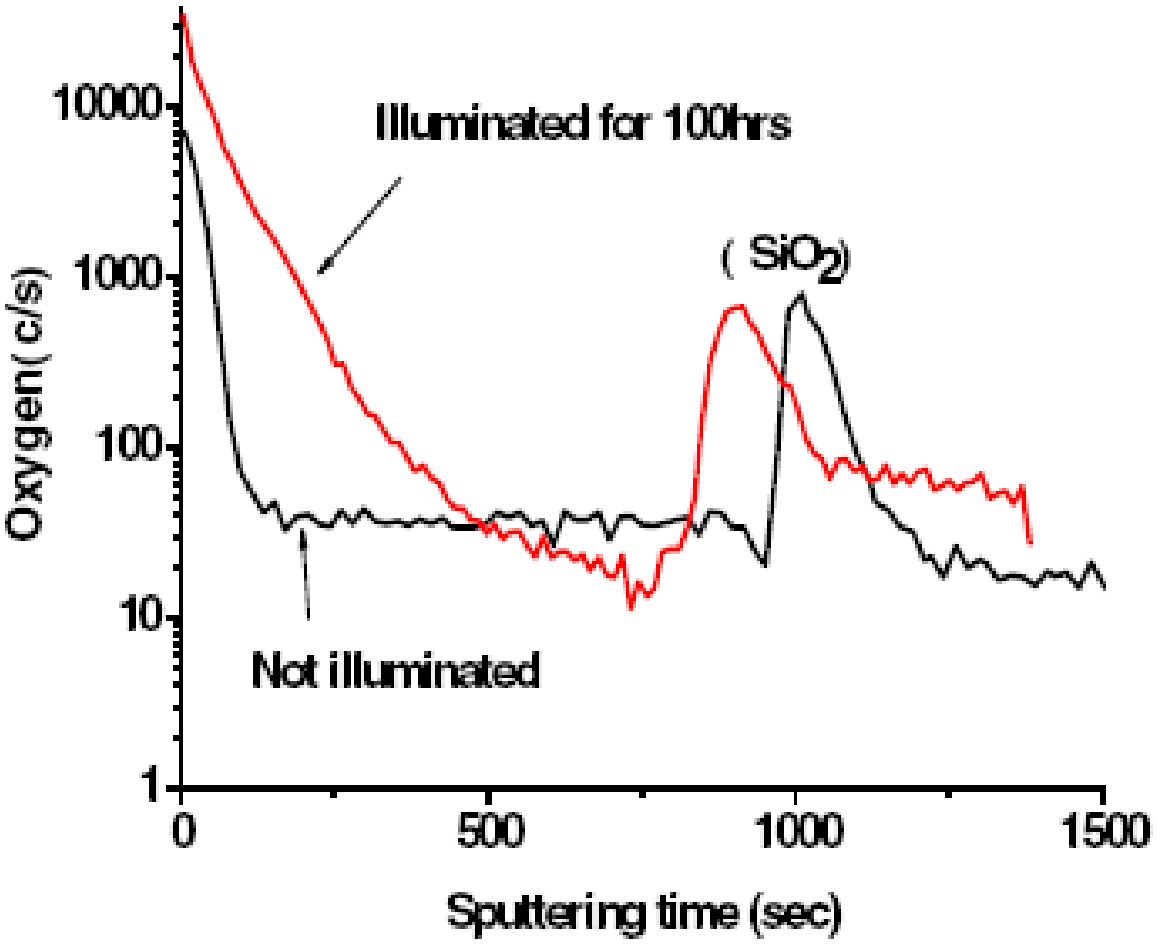
Illuminated for 100hrs
(SiO2)
Not illuminated
Oxygen(c/s)
10000
1000
100
10
1
0
500
1000
1500
Sputtering time (sec)

Figure 17

DISTRIBUTION LIST

DTIC/OCP 8725 John J. Kingman Rd, Suite 0944 Ft Belvoir, VA 22060-6218	1 cy
AFRL/VSIL Kirtland AFB, NM 87117-5776	2 cys
AFRL/VSIH Kirtland AFB, NM 87117-5776	1 cy
Official Record Copy AFRL/VSSE, Arthur Edwards	1 cy